

Uncertainty quantification of limit-cycle oscillations [☆]

Philip S. Beran ^{a,*}, Chris L. Pettit ^b, Daniel R. Millman ^c

^a *Multidisciplinary Technologies Center, Air Vehicles Directorate, AFRL/VASD,
Building 146, 2210 Eighth Street, WPAFB, OH 45433, USA*

^b *United States Naval Academy, 590 Holloway Rd., MS 11-B, Annapolis, MD 21402, USA*

^c *USAF TPS/EDT, 220 South Wolfe Ave, Bldg. 1220, Rm. 131, Edwards AFB, CA 93524-6485, USA*

Received 9 September 2005; received in revised form 29 March 2006; accepted 30 March 2006

Available online 30 June 2006

Abstract

Different computational methodologies have been developed to quantify the uncertain response of a relatively simple aeroelastic system in limit-cycle oscillation, subject to parametric variability. The aeroelastic system is that of a rigid airfoil, supported by pitch and plunge structural coupling, with nonlinearities in the component in pitch. The nonlinearities are adjusted to permit the formation of either a subcritical or supercritical branch of limit-cycle oscillations. Uncertainties are specified in the cubic coefficient of the torsional spring and in the initial pitch angle of the airfoil. Stochastic projections of the time-domain and cyclic equations governing system response are carried out, leading to both intrusive and non-intrusive computational formulations. Non-intrusive formulations are examined using stochastic projections derived from Wiener expansions involving Haar wavelet and B-spline bases, while Wiener–Hermite expansions of the cyclic equations are employed intrusively and non-intrusively. Application of the B-spline stochastic projection is extended to the treatment of aerodynamic nonlinearities, as modeled through the discrete Euler equations. The methodologies are compared in terms of computational cost, convergence properties, ease of implementation, and potential for application to complex aeroelastic systems.

Published by Elsevier Inc.

Keywords: Uncertainty quantification; Stochastic expansion; Polynomial chaos expansion; Harmonic balance; Limit cycle oscillation; Aeroelastic

1. Introduction

The desire to simulate limit-cycle oscillation (LCO) in aeroelastic systems has become increasingly practical over the last decade. While many significant challenges yet remain in modeling the phenomenon in a reliable and verifiable manner, there is little doubt that some of the key computational elements have taken shape. Recent work by Thomas et al. [36] and Farhat et al. [11] demonstrate that complex aeroelastic responses

[☆] The views expressed in this article are those of the authors and do not reflect the official policy or position of the United States Air Force, the Department of Defense, or the U.S. Government.

* Corresponding author. Tel.: +1 937 255 6645.

E-mail addresses: philip.beran@wpafb.af.mil (P.S. Beran), pettitcl@usna.edu (C.L. Pettit), daniel.millman@edwards.af.mil (D.R. Millman).

can be captured with Euler and Navier–Stokes analysis for geometry of practical significance. Additional work by Beran et al. [4] and Denegri and Dubben [8] exemplify the degree to which simulation with transonic small-disturbance theory can yield additional insights into the phenomenology of LCO.

Thomas et al. have commented on the sensitivity of computed LCOs to the modeled values of vehicle properties in their models [37]. They observed that small changes (<5%) in the natural frequencies of structural modes participating in the LCO of an F-16 caused large changes in LCO amplitude (>30%) and decrease of the speed of LCO onset (\approx 5%). This latter change, while seemingly small, represents a substantial and surprising reduction in the modeled operational capability of the vehicle. Their findings may indeed be a reflection of sensitivity of the actual phenomenon to real-world variations in the aeroelastic system. Currently, there exists a substantial flight-test program for the F-16 that helps to certify the vehicle for flight safety with any possible store configuration (i.e., externally mounted tank or munition) [5]. In many ways, the existence of this test program is a testimony to the sensitive degree to which the F-16's aeroelastic behavior depends on store properties such as weight, location, geometric shape (with or without fins), and airframe linkage. Within the test and evaluation community, there is much anecdotal knowledge concerning the variability in LCO response characteristics observed for fighter aircraft. An experimental study reported by Cunningham [6] examined how nominally identical aircraft could experience different aeroelastic responses based on variations in horizontal-tail structure within manufacturing tolerances.

Owing to the practical importance of avoiding or limiting LCO in operational vehicles, it is sensible to study the generic problem of computing the dependence of nonlinear oscillations on variations in system parameters. This effort serves to highlight some of the key computational issues through examination of idealized problems exhibiting LCO, and provides a roadmap for developing a more advanced capability suitable for real-world configurations.

While the literature is relatively rich in the stochastic analysis of problems that are either static, linear, or both, there is little work directed towards describing nonlinear processes that are dynamic with compact stochastic representations. Certainly, LCOs represent only one sub-class of dynamic processes; but they represent an important category of autonomous solutions that bifurcate from systems otherwise in equilibrium, and are the subject of study in many fields outside of the aerospace sciences. Furthermore, LCOs are challenging to simulate, in that the physical times needed to realize fully developed responses can be quite large. As it will be seen, this challenge is magnified when systems are analyzed stochastically.

Restricting the present review of stochastic analysis to those related to LCOs, comments on noteworthy features of several articles can be made. In a foundational effort, Xiu et al. [40] analyzed the stochastic response of a structurally supported cylinder in crossflow, subject to variability in structural stiffness. Assuming a Gaussian probability density function (PDF) for the random parameter, they computed PDFs of cylinder position at different time levels using Wiener expansions of the dependent variables in the specified random variable. These expansions will be described later, but yield a spectral (i.e., efficient) means for associating system response with values of input parameters, e.g., those selected in a sampling process. Stochastic solutions were tracked into the development of LCO, an aeroelastic phenomenon sustained in this problem by vortex shedding. Millman et al. [25] studied the LCO of a structurally supported airfoil in the time domain using modeled aerodynamics and a new Wiener expansion of the stochastic response with improved convergence properties. Focusing on the bifurcation characteristics of the system, nonlinearity of the torsional support was adjusted to yield a subcritical Hopf bifurcation, which enabled bi-modal responses to be analyzed.

In a set of papers in 2004, the authors and their colleagues studied the large-time failure of Wiener expansions in the time domain, and examined uniformly convergent means for characterizing uncertainty in LCO responses. First, Pettit and Beran [30] critically examined why stochastic analysis in the time-domain fails, using the previous airfoil problem. They found that the nonlinearity of the stochastic projection increases in time, such that any fixed projection becomes unsatisfactory in capturing the nonlinearity at a sufficiently large time. Beran and Pettit [2] proposed a non-time-domain approach to capturing LCO that is rapidly convergent, describing the stochastic behavior of the airfoil response in a very small number of orbital modes. In their work, one structural parameter, the cubic stiffness coefficient, was considered random. Millman et al. [26] alternatively proposed a stochastic projection method derived from B-splines and apply the technique to representing the probabilistic response of the airfoil in terms of a single output variable, the peak pitch angle. Two input variables were considered random, the cubic stiffness coefficient and the initial angle of attack. They

successfully reproduced the bi-modal characteristics of the response PDF, realizing that the aeroelastic state at large time would either be equilibrium (small initial angles) or LCO (large initial angles) for a range of reduced velocities. In turn, they used the compact B-spline representation with Monte-Carlo simulation (MCS) to predict quickly failure probability of the aeroelastic system (i.e., for peak pitch angle exceeding a threshold value) as a function of reduced velocity.

These studies, which sought to assess and employ spectral representations of the stochastic domain, were accompanied by other studies that probed the available range of aeroelastic behaviors through MCS. Pettit and Beran [29] investigated aeroelastic behaviors arising from variability in three input variables, the initial pitch angle and two stiffness coefficients. Lindsley et al. [19] examined the dynamic response of nonlinear panels in the presence of a distributed uncertainty in the material (the stiffness) and a parametric uncertainty in the support conditions, and later extended their work to include thermal effects [20]. Lindsley and Beran have also employed reduced order modeling with the proper orthogonal decomposition to accelerate the prediction of PDFs of panel response using MCS [21].

Recent studies expand the range of applications and techniques related to the stochastic analysis of LCOs. Attar and Dowell [1] employ MCS and a response surface method to map the output characteristics of a delta wing (as measured by the root-mean square of the wing tip displacement) to two input parameters considered variable: thickness and modulus of elasticity. As treated by Millman et al. [26], Attar and Dowell gave special attention in the response surface mapping to the modeling of the bifurcation leading to LCO. Pettit and Beran [32] continued study of the airfoil, and related oscillatory phenomena, using two-dimensional Wiener–Haar expansions. They found that the multiresolution properties of the Haar wavelet greatly increased the ability to capture properly stochastic aeroelastic properties with advancing time. Xiu et al. [41] provided an excellent assessment of the available expansion techniques for the stochastic domain, which they place in a category called stochastic Galerkin (SG) methods. Furthermore, they present a new, equation-free approach to capturing uncertainties in LCOs, based on a fixed-point formulation of the unsteady equations in LCO, like that previously examined by Beran and Pettit [2]. An important advantage of their equation-free formulation, as realized for a chemical reactor problem, is in preserving the strong convergence properties of SG methods while avoiding the need to make modifications to the deterministic algorithm to support the stochastic analysis (more will also be said on this subject later).

Finally, Pettit and Beran [33] examined new challenges to methodology development and uncertainty assessment arising from the need to treat distributed variability. While the bulk of the prior work on dynamical systems addressed parametric uncertainty (and for a very limited number of parameters), practical systems will be characterized by random fields and/or large, discrete sets of random parameters. The issues deemed by Pettit and Beran to be of critical interest were how to measure the influence of grid quality on statistical properties of the response, such as skewness, and how to apply SG methods to models described by a very large number of input parameters.

This paper is an exposition of the authors' joint study of uncertainties in LCO, which unites the presentation of the examined computational methodologies in a manner enabling the reader to discern the relative strengths and weaknesses of the different techniques. The unpublished content of this paper primarily draws from work related to the extension of so-called cyclic analysis to stochastic systems in LCO, a subject concentrated on in this work. First, a common set of principles and nomenclature are introduced and applied to the formulation of the stochastic methods, starting with a description of the airfoil problem, which serves as an application backbone for the paper. Results for this problem are then presented, with attention primarily given to the dependence of LCOs erupting from subcritical Hopf bifurcations on input parameters considered to be random. Lastly, properties of the schemes are contrasted, and commentary on future needs for methodology development is given.

2. Formulation

This article attempts to unite the discussion of different approaches for characterizing uncertainties in LCOs; a typical aeroelastic problem serves as a common reference point for the different threads of the dialogue. Each of the techniques requires description, to some appropriate level, of a mathematical frame-

work. To help guide the reader in studying the aeroelastic problem and the stochastic techniques of interest, the following outline is provided. It should be noted that Sections 2.4 and 2.5 pertain to dynamic responses that characterize the entire LCO, while Section 2.6 restricts attention to LCO amplitude.

- Sec. 2.1 The Aeroelastic model problem
- Sec. 2.2 Deterministic analysis of the model problem
- Sec. 2.3 Mathematical representations of the stochastic dimension
- Sec. 2.4 Stochastic LCO responses: a non-time-domain approach
- Sec. 2.5 Stochastic LCO responses: a time-domain approach
- Sec. 2.6 Stochastic LCO amplitudes: a projection approach

2.1. Airfoil problem

The aeroelastic system studied here is a nonlinear incarnation of the standard symmetric airfoil in low-speed flow, described by two physical degrees of freedom (DOFs): pitch, $\alpha(t)$, and plunge, $h(t)$ (see Fig. 1). The current formulation is an extension of that investigated previously by Lee et al. [16] in which the plunge DOF has linear stiffness but the pitch DOF includes a 3rd-order stiffness term in addition to the linear component. For their model, the restoring force associated with the torsional spring is expressed as $K_\alpha(\alpha + k_3\alpha^3)$, where K_α is the dimensional linear stiffness and k_3 is the dimensionless parameter governing the cubic nonlinearity. In the stochastic analysis reported later in this paper, k_3 is related to a random variable.

When the system is fully linear ($k_3 = 0$), the onset of unbounded growth aeroelastic oscillations, otherwise known as “flutter”, occurs at a Hopf bifurcation located at λ^* , where λ is defined to be a nondimensional parameter proportional to flight speed (“reduced velocity”). In physical systems, aeroelastic responses are linearly stable below the critical speed but linearly unstable above the critical speed. In the model, positive values of k_3 yield a supercritical Hopf bifurcation, for which stable LCOs are sustained for $\lambda > \lambda^*$, while negative values of k_3 represent a situation of spring softening for which the bifurcation is subcritical and unstable LCO states exist for $\lambda < \lambda^*$.

In the current study, a 5th-order element to the pitch restoring force is added, $K_\alpha k_5 \alpha^5$, following previous work [29]. With this form of the torsional stiffness, selection of $k_3 < 0$ and $k_5 > 0$ yields a subcritical bifurcation that possesses a cyclic fold at λ^{LCO} such that stable LCO states are available for $\lambda > \lambda^{\text{LCO}}$, where $\lambda^{\text{LCO}} < \lambda^*$. The final form of the 8-DOF system is given elsewhere [28]. A FORTRAN-90 subroutine by which $\mathbf{f}(\mathbf{x})$ is evaluated is available from the first author upon request.

The airfoil dynamics are represented by a small system of eight ODEs, obtained in compact form through linear modeling of the aerodynamics [16]. The nonlinear, autonomous equations are written in a generic form as

$$\frac{d\mathbf{x}}{dt} = \mathbf{f}(\mathbf{x}; \lambda, \gamma), \quad (1)$$

where γ is a system parameter that will be varied, and \mathbf{x} is the array of dependent variables, such that $\mathbf{x} \in \mathbb{R}^N$, where here $N = 8$. \mathbf{f} is an array of nonlinear equations such that $\mathbf{f} : \mathbb{R}^N \times \mathbb{R}^2 \rightarrow \mathbb{R}^N$. The notation of placing

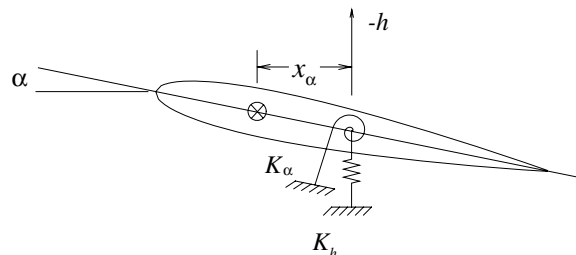


Fig. 1. Schematic of pitch-and-plunge airfoil.

arrays in boldface is adopted herein. It should also be noted that γ can be generalized to include additional parameters of relevance.

The solution of (1) is subject to the initial conditions

$$\mathbf{x}(t = 0) \equiv \mathbf{x}_0, \quad (2)$$

where the initial conditions can be parameterized as well.

A more sophisticated model of the aeroelastic airfoil, which employs computational fluid dynamics (CFD) to predict airloads, has been applied in stochastic analysis by Millman [28]. The CFD methodology is based on the discrete Euler equations, and the airfoil is structurally supported using the Pettit and Beran cubic/pentic formulation [29] described above. While the dimensionality of the CFD-based analysis is much greater, the generic representation of the aeroelastic system, (1), remains unchanged. For reference, the grid used in the Euler analysis, which corresponds to a NACA 64A006 airfoil, is shown in Fig. 2. When results are shown later for this model, it will be referred to as the airfoil/CFD problem.

2.2. Deterministic analysis of the governing equations

The system of equations (1) is straightforward to time integrate with either explicit or implicit techniques. The integration proceeds from the initial state to a time t at which the solution is deemed to be in steady-state or LCO. Details of various techniques are given in [3,28].

A representative time history is shown in Fig. 3, as obtained by time integrating the low-order airfoil model for a spring-hardening case ($\lambda = 6.35$; other model specifics are given in Section 3). Response in pitch angle is shown. For this supercritical case, the evolution towards LCO is relatively slow, and can be made slower by decreasing λ towards λ^* . Analysis of (1) proceeds in a time-accurate fashion over these many cycles, starting from the initial time $t = 0$.

Now, the equations are re-cast and expanded into a form that we refer to as “cyclic”, A basic cyclic method, well suited for the low-order nature of the problem, is described that is later extended into a stochastic form. Details of the methodology development and application were described elsewhere for deterministic systems, with emphasis on reduced order modeling as a potential strategy for enabling analysis of large sets of equations [2]. Further comments on the background of the method are made later in the section, along with a discussion of the context of the methodology with respect to other useful methods.

In cyclic form, time-periodic solutions of (1) are sought that satisfy

$$\mathbf{x}(t) = \mathbf{x}(t + T), \quad (3)$$

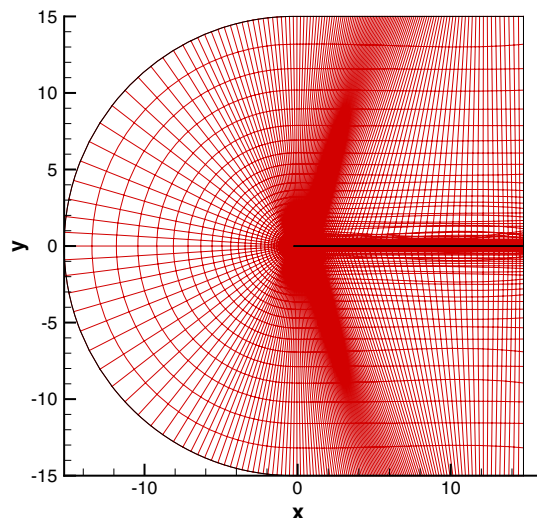


Fig. 2. Grid used by Millman [27] for Euler analysis of airloads on airfoil.

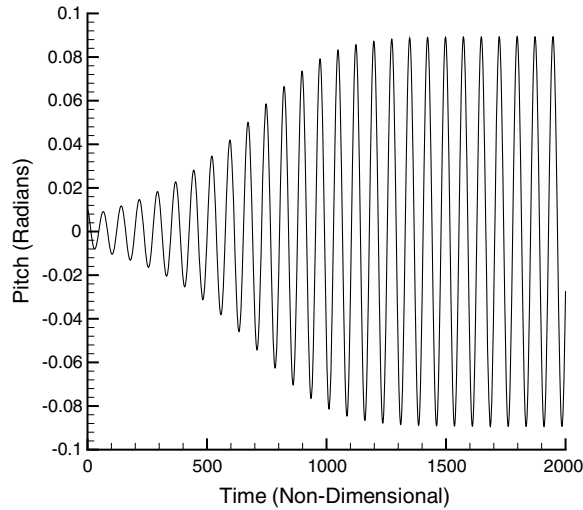


Fig. 3. Response of airfoil in time for a supercritical LCO ($\lambda = 6.35$, see Section 3).

where T is the period of the assumed LCO. The time variable is scaled, $s \equiv t/T$, leading to an equation in which the period appears explicitly:

$$\frac{d\mathbf{x}}{ds} = T\mathbf{f}(\mathbf{x}; \lambda, \gamma). \quad (4)$$

A set of points on the periodic orbit at N_t uniformly distributed time levels is selected, leading to an expanded array of $N_t N$ unknowns,

$$\mathbf{X} \equiv (\mathbf{X}_1, \mathbf{X}_2, \dots, \mathbf{X}_{N_t})^T = (\mathbf{x}(s_1), \mathbf{x}(s_2), \dots, \mathbf{x}(s_{N_t}))^T,$$

where here the subscript specifies the time level (i.e., $s_{j+1} = s_j + \Delta_s$; $\Delta_s \equiv 1/N_t$). Using the trapezoidal rule, (1) is discretized with 2nd-order accuracy at each of the temporal points on the orbit to yield an expanded collection of equations ($j = 1, \dots, N_t$):

$$\mathbf{G}_j \equiv \frac{1}{2}(\mathbf{F}_{j+1} + \mathbf{F}_j) - \frac{1}{\Delta_s}(\mathbf{X}_{j+1} - \mathbf{X}_j) = 0, \quad (5)$$

where $\mathbf{F}_j \equiv T\mathbf{f}(\mathbf{x}(s_j))$. A closed set of equations,

$$\mathbf{G} \equiv (\mathbf{G}_1, \mathbf{G}_2, \dots, \mathbf{G}_{N_t}, \mathbf{G}_{N_t+1}, \mathbf{G}_{N_t+2})^T = 0, \quad (6)$$

is obtained by adding a pair of scalar constraints to (6) to prevent the solution from being trivial (i.e., $\mathbf{X}_j = 0$ for all j) and to prevent the phase of the solution to be arbitrary:

$$\mathbf{G}_{N_t+1} \equiv (\mathbf{X}_j)_{i_1} - \beta_1 = 0, \quad (7)$$

$$\mathbf{G}_{N_t+2} \equiv (\mathbf{X}_j)_{i_2} - \beta_2 = 0, \quad (8)$$

where j is an arbitrary point on the cycle, usually taken to be 1, and i_1 and i_2 are indices corresponding to two different variables at that time instant. Constraint (7) is used to identify the “starting” point of the cycle, such that $\beta_1 = 0$ (assuming an oscillation approximately centered about 0 for the selected variable). Likewise, (8) is used to set the amplitude of the cycle, such that $\beta_2 \neq 0$. For this study, $i_1 = 1$ and $i_2 = 2$. These constraints are graphically depicted in Fig. 4, which shows a 16-point cycle in a two-parameter phase space that is assumed to progress in a counter-clockwise fashion in time.

The addition of two equations is accompanied by an increase in the number of unknowns by two. These unknowns are $\mathbf{X}_{N_t+1} = \lambda$ and $\mathbf{X}_{N_t+2} = T$. Thus, a total of $N_t N + 2$ equations are solved for not only the LCO solution, but also the period of the oscillation and the value of the free parameter λ at which the

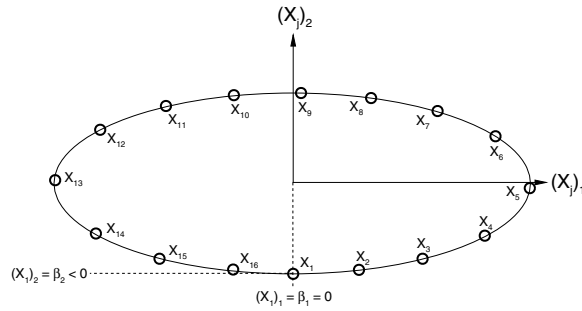


Fig. 4. LCO described by 16 points in $(X_j)_1$ – $(X_j)_2$ phase plane, assuming counter-clockwise progression.

LCO meets the amplitude constraint (8). This inverse approach of specifying the amplitude and computing the physical parameter we refer to as the cyclic specified amplitude (CSA) method.

In symbolic form, the complete system of cyclic equations is expressed as

$$\mathbf{G}(\mathbf{X}; \lambda, \gamma, \beta_1, \beta_2) = 0, \tag{9}$$

and is solved for an expanded form of \mathbf{X} ,

$$\mathbf{X} \equiv (\mathbf{X}_1, \mathbf{X}_2, \dots, \mathbf{X}_{N_t}, \lambda, T)^T, \tag{10}$$

using Newton’s method and Gaussian elimination. The Jacobian, \mathbf{J} , of the system is formulated numerically using a one-sided difference approximation. To close (9), periodicity must be enforced, which is accomplished in (5) by replacing references to \mathbf{X}_{j+1} at point N_t by \mathbf{X}_1 . With this modification, and the additional constraint equations, \mathbf{J} becomes a bordered, banded matrix.

It should be pointed out that while time accuracy is maintained in this iterative process through the time discretization implicit to $\mathbf{G} = 0$, time accuracy is not maintained from one orbit to the next. For LCOs that develop slowly, placement of the equations in steady-state form can greatly accelerate convergence to the correct LCO solution. This observation that time accuracy is not needed to compute \mathbf{X} has some other interesting implications. From a computational perspective, \mathbf{X} is not necessarily dependent on \mathbf{x}_0 (the initial conditions); any initial guess of the asymptotic solution behavior may serve as an initial condition, provided that the iterative process is convergent.

Assuming convergence, the numerical procedure will behave differently for supercritical and subcritical bifurcations. As depicted in Fig. 5, different branches of deterministic LCO solutions are possible (taking λ as a free variable), and form the backbone of clusters of neighboring LCO solutions arising from reasonable variations of parameters in the nonlinear model. For supercritical bifurcations, the procedure will converge to a single LCO for a specified amplitude on the supercritical branch. This is consistent with the physical

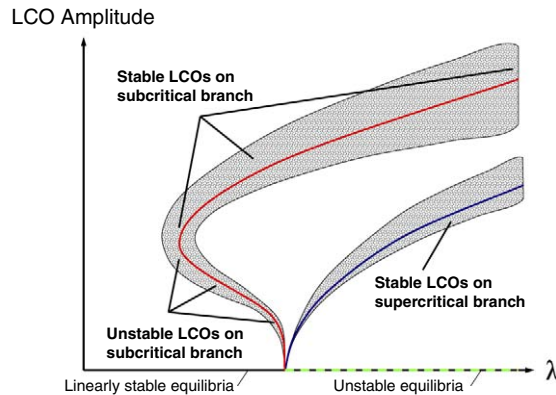


Fig. 5. Cartoon of possible branches of LCO solutions from a simple Hopf bifurcation point, subject to variability in the nonlinear dynamics (deterministic solutions shown as curves, stochastic solutions shown as cross-hatched clusters).

response, in that all initial conditions are attracted by the same stable LCO. However, for subcritical LCOs, there exists a range of values of λ for which $\mathbf{G} = 0$ is satisfied by two distinct LCOs of different amplitudes, one physically stable and one physically unstable, as well as equilibrium solutions that are linearly stable. Thus, for a subcritical bifurcation, LCO amplitudes can be specified that lead to solutions \mathbf{X} that are not physically realizable. Furthermore, in this same range of λ , equilibrium solutions are stable, again depending on initial conditions. It follows that for this kind of bifurcation, cyclic methods do not connect solutions and initial conditions in a physically consistent manner.

The CSA method provides a means for computing starting points on branches of LCO solutions by enforcing an amplitude condition not achievable by the trivial solution $\mathbf{f} = \mathbf{x} = 0$. In general, it is difficult to “move off” the branch of trivial static solutions near a bifurcation point through Newton iterates of (9) without forcing the LCO amplitude to be non-trivial. However, once a converged, non-trivial LCO solution is computed with the CSA method, the solution can be used as an initial guess for a similar calculation in which λ is specified. This direct approach of specifying the physical parameter and computing the LCO amplitude we refer to as the cyclic specified parameter (CSP) method, and is simply implemented by removing (8) from the set of equations (9) or by replacing (8) with the equation $\lambda - \bar{\lambda} = 0$ where $\bar{\lambda}$ is the target value of λ . Thus, with the CSP method, the equations are essentially expressed as

$$\mathbf{G}(\mathbf{X}; \bar{\lambda}, \gamma, \beta_1) = 0. \quad (11)$$

A representative cyclic solution is shown in Fig. 6, as obtained by solving the CSA equations for a spring-softening case ($\lambda \approx 7$; other model specifics are given in Section 3). Linked responses in pitch angle and plunge are shown. The gap in the curve represents the index cut between the first and last points collocated into \mathbf{X} .

We conclude this section with a brief discussion of the methods developed to solve (1), subject to (3). The current formulation, a 2nd-order-accurate finite-difference method [3], is not new, but directly inspired by the previous work of Doedel [9] (creator of AUTO) and others, e.g. [15]. As will be shown, the application of this approach in the stochastic domain resolves certain mathematical problems in a manner that is considered by the authors to be new. As a finite-difference technique, the CSA method can be regarded as an H -convergent process, where H is used here to denote time-point spacing (h is widely regarded in the literature to represent grid-point spacing, but is reserved herein for plunge). P -convergent methods based on Fourier expansions, otherwise known as “harmonic balance” (HB) have been developed for, and applied to, aeroelastic and turbo-machinery problems. The interested reader is urged to consult the following Refs. [14,10,23,35]. For self-excited oscillations, a critical aspect of the computation is in the accurate prediction of the time period. So far, that component of the LCO computation has not been robustly and seamlessly handled in the various available schemes. The current method provides strong convergence to the LCO solution, including the per-

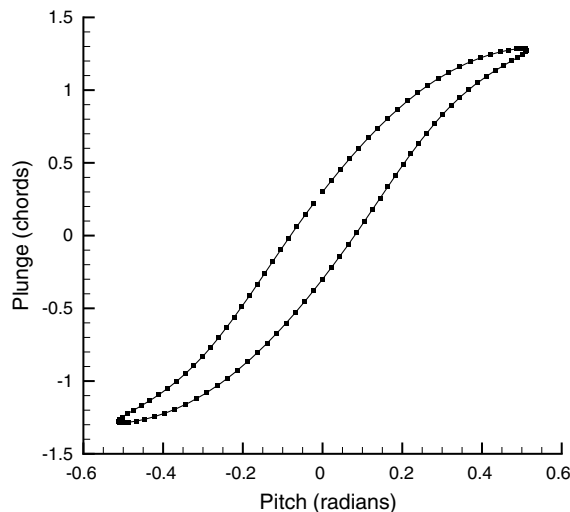


Fig. 6. Cyclic solution obtained for airfoil problem near $\lambda = 7$.

iod, but only for the simple problems to which it has been applied. Application to more complex problems will likely require significant algorithmic modifications.

2.3. Preliminaries concerning chaos expansions of stochastic processes

To this point, a problem has been defined involving a deterministic, physical process connecting a set of known input conditions to a calculable system response. The problem of interest, however, involves values of input conditions that are not known, but which have some probability of falling within certain intervals. To aide in re-casting the problem in stochastic form, e.g., enabling Wiener (spectral) expansions in terms of stochastic variables, some well-known mathematics are reviewed. This review follows that put forward by Pettit and Beran [30]. Ghanem and Spanos [13] provide a complete exposition of the theory by which the polynomial chaos expansion, one of the most well known Wiener expansions, is developed.

2.3.1. Probability background

We assume θ is an outcome in a probability space, $\zeta(\theta)$ is a random variable (rv) that maps outcomes from the probability space to \mathbb{R} , and $y \in \mathbb{R}$ is a possible value of ζ . This rv follows a specified distribution function,

$$M_{\zeta}(y) = Pr[\theta : \zeta(\theta) \leq y], \tag{12}$$

where Pr quantifies the portion of the probability space for which the values of the rv do not exceed y . We assume that $M_{\zeta}(y)$ is continuous and strictly increasing. Under these conditions, $dM_{\zeta}(y) = m_{\zeta}(y) dy$ defines the probability density induced by $\zeta(\theta)$.

Before proceeding, some comments need to be made concerning notational conventions. It is common in the literature regarding stochastic processes to denote a random process by a capital letter, e.g., W , and a realization of the process by the same letter in lower case, e.g., w . We sacrifice this convention in the current paper, since capital letters have been used to denote cyclic variables. In this sense, an individual realization of the cyclic process will be denoted by $X_i(y)$.

The expected value operator of the process x_i for any time t is written as

$$Ex(t) = \langle x_i(t, \zeta) \rangle = \int x_i(t, \zeta(\theta)) Pr(d\theta) = \int_{-\infty}^{\infty} x_i(t, y) m_{\zeta}(y) dy. \tag{13}$$

2.3.2. Global bases for the stochastic dimension

A general Wiener expansion provides a spectral means for decomposing a 2nd-order random process when the covariance operator is unknown, as is the case for the response of a nonlinear system. Assuming one rv, the Wiener expansion of $x_i(t)$, the i th component of the aeroelastic response, is expressed as

$$x_i(t, \zeta(\theta)) = \sum_{j \in J} [\hat{x}_i]_j(t) \Psi_j(\zeta(\theta)), \tag{14}$$

where $\{\Psi_j(\zeta(\theta))\}$ is a set of basis functions that are orthogonal (more will be said about orthogonality later) with respect to the distribution of ζ , and M is an index set whose structure depends on the type of basis. For example, this paper will consider 1-D spectral expansions involving Hermite polynomials and B-splines, and 2-D expansions involving Haar wavelets. In turn, an input variable that is assumed random is also represented by Wiener expansions:

$$\gamma(\zeta(\theta)) = \sum_{j \in J} \hat{\gamma}_j \Psi_j(\zeta(\theta)). \tag{15}$$

For notational convenience, the expansions above are shown in terms of one rv (ζ), which can be thought of as an additional problem dimension. In general, however, for a given problem, any number of rv's can be present, greatly increasing the number of potential expansion coefficients.

A spectral expansion based on the Hermite polynomials, $He_j(\zeta)$, is referred to as the Wiener–Hermite (WHE) expansion, the Hermite chaos, or polynomial chaos expansion (PCE), which was popularized by Ghanem and Spanos [13]. This expansion is particularly useful for representing Gaussian processes, since the basis functions are statistically orthogonal with respect to the Gaussian measure, i.e.,

$$\langle \text{He}_i, \text{He}_j \rangle \equiv \frac{1}{2\pi} \int_{-\infty}^{\infty} \text{He}_i(\xi) \text{He}_j(\xi) e^{-\xi^2/2} d\xi = 0 \quad (i \neq j), \quad (16)$$

where $\frac{1}{2\pi}e^{-\xi^2/2}$ is the probability density function associated with an rv that is Gaussian. The polynomials are constructed from the recurrence relation

$$\text{He}_0(\xi) = 1, \quad \text{He}_1(\xi) = \xi, \quad \text{He}_j(\xi) = \xi \text{He}_{j-1} - (j-1) \text{He}_{j-2}, \quad (17)$$

and satisfy $\langle \text{He}_i, \text{He}_i \rangle = i!$.

If the rv is uniformly distributed on a finite interval, a similar expansion can be employed with the Legendre polynomials as the basis: the Wiener–Legendre (WLe) expansion. The WLe development is omitted, because it directly parallels that which is presented here for WHe. Spectral expansions for other probability distributions and their associated bases have recently appeared [39,17]. It is noted that use of an expansion that is not well suited to the character of the underlying rv will typically result in poor performance of the selected expansion.

When employed in stochastic analysis, the WHe is truncated to include $P + 1$ terms:

$$\gamma(\xi(\theta)) = \sum_j^P \hat{\gamma}_j \text{He}_j(\xi(\theta)). \quad (18)$$

The expansion in (18) is guaranteed to converge as $P \rightarrow \infty$ for any square-integrable process, where square-integrable is with respect to the Gaussian probability measure.

In this paper, rv's will be considered to be either standard normal, i.e., Gaussian with vanishing mean and of unity standard deviation, or uniform over the unit interval. The latter is specified in the case of wavelet expansions. In the case of standard normal rv's, related input parameters are taken to be Gaussian, such that

$$\gamma = \gamma_0 + \gamma_1 \xi, \quad (19)$$

which is a two-term WHe expansion.

2.3.3. Projection techniques for the stochastic dimension

Given one of the expansions provided above, a stochastic representation of the desired response is obtained when the coefficients in the expansion are known. Methods for computing these coefficients fall into two categories: non-intrusive and intrusive. The former class of methods involves sampling solution behavior for different values of ξ and then numerically inverting (14) to obtain the coefficients. This approach does not require modification of the deterministic algorithm that generates responses, but does require an appropriate interrogation of the sampling space.

For example, consider a WHe expansion of the response, $x_i(t, \xi)$:

$$x_i(t, \xi(\theta)) = \sum_{j \in J} [\hat{x}_i]_j(t) \text{He}_j(\xi(\theta)). \quad (20)$$

Then, following a SG projection of both sides of (20), and exploiting the orthogonality properties of the Hermite polynomial, the WHe coefficients are expressed in terms of an expected value computation (removing the explicit appearance of θ):

$$[\hat{x}_i]_j(t) = \frac{1}{j!} \langle x_i(t, \xi) \text{He}_j(\xi) \rangle. \quad (21)$$

$[\hat{x}_i]_0(t)$ represents the time-dependent, expected value of the process, and $\sum_{j=1}^P ([\hat{x}_i]_j(t))^2$ approaches the time-dependent variance as $P \rightarrow \infty$.

Standard Monte-Carlo simulation (MCS) can be employed to estimate the expected value in (21). This simple procedure involves generating N_{MCS} realizations of ξ , computing the associated set of realizations of $\mathbf{x}(t, \xi)$ from the physical model, and estimating (21) at each time step for each expansion coefficient and each component of \mathbf{x} . More efficient approaches that could be considered for practical implementation include the many variance reduction or efficient sampling techniques [24], which should improve the convergence of the MCS, and Gauss–Hermite quadrature of the integral in (14). Given the computational expense associated with realistic aeroelastic simulations, some combination of efficient sampling and reduced-order physics models will likely be required for more complex problems. Pettit [31] discusses this in slightly greater depth.

Intrusive methods involve the projection of the governing equations onto the Wiener basis followed by numerical calculation of solutions to the projected equations. Such methods, essentially Galerkin formulations over the stochastic domain, do involve modification of the deterministic algorithm, but produce stochastic solutions in “one-shot” without the need for sampling. Ghanem and Spanos [13] provide the details of an intrusive formulation for a linear, finite element formulation and Millman, et al. [28] take this path for the airfoil problem outlined at the start of this section. In many ways, however, intrusive methods resemble non-intrusive methods in that expected values need to be computed. The question of which formulation is more computationally efficient is primarily determined by the speed with which expected values of terms appearing in the governing equations can be computed. For the intrusive approach to be superior, the expected value computation must be accelerated by taking advantage of the known form of the governing equations.

2.3.4. Failure of global bases for time-domain stochastic LCO analysis

Drawing from the material developed above, it would seem to be a simple task to analyze LCO time series derived for different values of a relevant random parameter (ξ), and then construct the WHe coefficients in time, following (21). Pettit and Beran carried out this task for the airfoil problem [30] and found the surprising result that the WHe expansion failed at sufficiently large times, as exhibited by a growing reduction in the energy contained within the reconstructed solution with increasing time. This behavior is shown in Fig. 7 for a case of supercritical LCO by comparing the deterministic solution (baseline) to solutions reconstructed from WHe projections using 3rd-order, 10th-order, and 20th-order expansions. Solutions are shown at large time (i.e., numerous periods of oscillation). Clearly, the expansions fail in reproducing the baseline result (for $\xi = 0$). Pettit and Beran [30] and Millman et al. [26] describe the computational problems associated with the WHe expansions in greater detail, but point to the failure of fixed-order WHe expansions at large-time to capture an increasing level of nonlinearity in the dependence of $x_i(t, \xi)$ on ξ .

Similar findings are reported by Wan and Karniadakis [38], who developed an adaptive, multi-element basis to combat errors in the stochastic analysis that appear at large time, like that described above. Their procedure also provides a means for capturing discontinuities in system response within a framework of stochastic analysis. This capacity has relevance to our later discussion of discontinuities in LCO response, which arise when the biurcation behavior is subcritical.

2.3.5. Local bases for the stochastic dimension

The Haar wavelet is now introduced, whose basis constitutes the most elementary multi-resolution analysis (MRA) of $L^2(\mathbb{R})$ [12], the set of square-integrable real-valued functions on \mathbb{R} . This basis is used to resolve the highly nonlinear behavior of the LCO response in the stochastic domain to address the failure observed in the last section. The presentation follows that of [34], where additional details can be found.

The Haar scaling function is defined by

$$\phi(v) = \mathbf{I}_{[0,1)}(v) = \begin{cases} 1, & 0 \leq v < 1, \\ 0, & \text{otherwise,} \end{cases} \quad (22)$$

where $\mathbf{I}_{[a,b)}(v)$ is the indicator function for $v \in [a,b)$. Scaled and translated versions of $\phi(v)$ are written as

$$\phi_k^{(j)} = 2^{j/2} \phi(2^j v - k), \quad (23)$$

where $j \in \{\mathbb{Z} \geq 0\}$, \mathbb{Z} is the set of integers, $k \in [0, 2^j - 1]$, and the scale factor, $2^{j/2}$ is chosen so that $\|\phi_k^{(j)}\| = 1$.

Let $z(v)$ be a square-integrable, real-valued function on the unit interval. Each scale or dilation factor j defines a function space, $V_j = \text{span}\{\phi_k^{(j)}\}$ such that $V_{j-1} \subset V_j$. The set $\{\phi_k^{(j)}\}$ forms a partition of $[0,1)$. Let $P^{(j)}z$ be the projection of z onto V_j ; then

$$P^{(j)}z = \sum_{k=0}^{2^j-1} c_k^{(j)} \phi_k^{(j)}(v), \quad (24)$$

and the projection coefficients are given by the inner product

$$c_k^{(j)} = \int_0^1 z(v) \phi_k^{(j)}(v) \, dv. \quad (25)$$

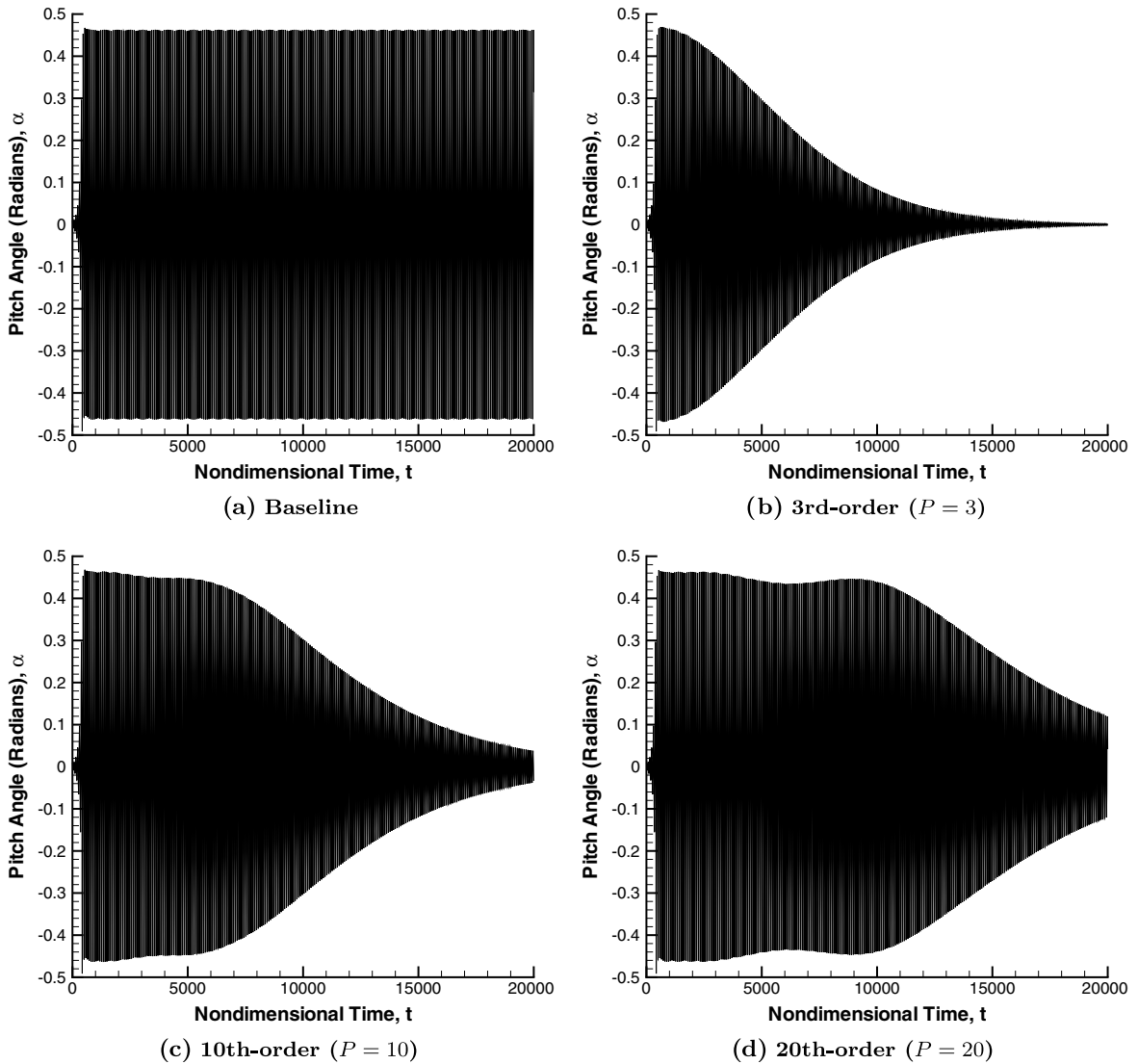


Fig. 7. Baseline airfoil LCO and simulated limit cycles computed from WHe expansions ($\xi = 0$).

Increasing j therefore produces a higher resolution projection, so that the sequence of spaces $\{V_j\}_{j=0}^\infty$ comprise a MRA of $L^2([0,1])$. Scaling the unit interval extends this to a MRA of $L^2(\mathbb{R})$. The projection $P^{(j-1)}z$ leaves behind a detail function $w^{(j-1)} \in V_j$, which is the difference between two resolution levels:

$$w^{(j-1)} = P^{(j)}z - P^{(j-1)}z. \tag{26}$$

This difference can be represented in terms of the Haar wavelets, which are based on the piecewise-constant mother wavelet:

$$\psi(v) = \begin{cases} 1, & 0 \leq v < 1/2, \\ -1, & 1/2 \leq v < 1, \\ 0, & \text{otherwise.} \end{cases} \tag{27}$$

An orthonormal basis for $L^2(\mathbb{R})$ is composed of all possible integer-valued translations and dilations of $\psi(v)$,

$$\psi_k^{(j)}(v) = 2^{j/2}\psi(2^jv - k), \quad j, k \in \mathbb{Z}, \tag{28}$$

which satisfy $\|\psi_k^{(j)}(v)\| = 1$; therefore, any square-integrable function can be expanded in a doubly indexed Haar wavelet series,

$$z(t) = \sum_{j,k} d_k^{(j)} \psi_k^{(j)}(v), \tag{29}$$

and the generalized Fourier coefficients can be evaluated as

$$d_k^{(j)} = \int_{-\infty}^{\infty} z(v) \psi_k^{(j)}(v) \, dv. \tag{30}$$

The detail function can be synthesized from the wavelets at scale $j - 1$,

$$w^{(j-1)} = \sum_{k=0}^{2^{j-1}-1} d_k^{(j-1)} \psi_k^{(j-1)}(v), \tag{31}$$

and the projection $P^{(j)}z$ can be expanded as

$$\begin{aligned} P^{(j)}z &= P^{(j-1)}z + \sum_{k=0}^{2^{(j-1)}-1} d_k^{(j-1)} \psi_k^{(j-1)}(v) \\ &= P^{(0)}z + \sum_{m=0}^{j-1} \sum_{k=0}^{2^m-1} d_k^{(m)} \psi_k^m(v) \end{aligned} \tag{32}$$

$$= c_0 \phi(v) + \sum_{m=0}^{j-1} \sum_{k=0}^{2^m-1} d_k^{(m)} \psi_k^m(v). \tag{33}$$

In practice, the upper resolution limit, $J = \max(j)$, must be determined by the resolution needed to retain the scales that contain significant energy.

2.4. Wiener–Hermite cyclic analysis

The CSP method can be used to establish the dependence of limit cycle behavior on system parameters, and evaluate the probabilistic system response subject to variability in these key parameters. For the time being, Gaussian variability in a single parameter, γ , is considered, such that

$$\gamma = \hat{\gamma}_0 + \hat{\gamma}_1 \zeta, \tag{34}$$

where ζ is an rv, and $\hat{\gamma}_0$ and $\hat{\gamma}_1$ are constants. Later, the problem of two random input variables is discussed.

In this manner, (11) is now expressed as

$$\mathbf{G}(\mathbf{X}; \bar{\lambda}, \gamma(\zeta), \beta_1) = 0, \tag{35}$$

which governs the random process defining the system response, $\mathbf{X}(\bar{\lambda}, \zeta)$. Eq. (35) is written in a form that recognizes the underlying dependence of \mathbf{G} on ζ through γ . As discussed above, the stochasticity of the system can be inferred with MCS, using actual realizations of the LCO solution for specified values of $\bar{\lambda}$. However, a more efficient, and perhaps variance reducing, approximate approach is to represent the random process by a truncated series expansion in the stochastic dimension:

$$\mathbf{X}(\bar{\lambda}, \zeta) = \sum_{i=0}^P \widehat{\mathbf{X}}_i(\bar{\lambda}) \text{He}_i(\zeta). \tag{36}$$

For the projected stochastic CSP (PSCSP) method, the coefficients of the PCE, $\widehat{\mathbf{X}}_i(\bar{\lambda})$, can be evaluated from a set of actual LCO realizations by applying the expected value operation, $\langle \cdot \rangle$, and orthogonality to (36):

$$\widehat{\mathbf{X}}_i(\bar{\lambda}) = \frac{1}{i!} \langle \mathbf{X} \text{He}_i \rangle. \tag{37}$$

Once $\widehat{\mathbf{X}}_i$ are computed, then “simulated” realizations of $\mathbf{X}(\bar{\lambda})$ can be obtained by evaluating (36) for random values of ξ . Branches of coefficient solutions can be found through repeated application of the process for different values of $\bar{\lambda}$.

The PSCSP method is applied to the solution data generated by the CSP method and thus is non-intrusive. Also of interest are the relative merits of the PSCSP approach with respect to an alternative, intrusive approach (ISCSP), where variability is accounted for by making fundamental changes to the CSP method. The goal of the ISCSP process is the direct computation of PCE coefficients for each of the N_t points in a stochastic LCO. First, an extended solution array, $\widehat{\mathbf{X}}(\bar{\lambda})$, is defined that contains all the cyclic PCE coefficients:

$$\widehat{\mathbf{X}} \equiv (\widehat{\mathbf{X}}_0, \widehat{\mathbf{X}}_1, \dots, \widehat{\mathbf{X}}_P)^T, \quad (38)$$

where $\widehat{\mathbf{X}}_i$ are the i th-order PCE coefficients corresponding to \mathbf{X} . In implementing the ISCSP method, three indices are defined to reference the $N \times N_t \times P + 1$ variables comprising $\widehat{\mathbf{X}}$: i , the index corresponding to the PCE order; j , the index corresponding to point on the LCO, and k , the index corresponding to the k th element of \mathbf{x} at the j th LCO point.

An expanded set of equations are solved to compute all the unknowns associated with $\widehat{\mathbf{X}}$. These equations are formulated by taking expected values of $\mathbf{G}\mathbf{H}\mathbf{e}_i$ (where \mathbf{G} is evaluated using the PCE-approximated form of \mathbf{X}) for each of the N_m components of the PCE, and enforcing (11):

$$\langle \mathbf{G}\mathbf{H}\mathbf{e}_i \rangle = 0, \quad i = 0, \dots, P. \quad (39)$$

Eq. (39) is assembled into a single set, expressed as

$$\widehat{\mathbf{G}}(\widehat{\mathbf{X}}; \bar{\lambda}, \gamma, \beta_1) = 0, \quad (40)$$

in a manner consistent with the construction of $\widehat{\mathbf{X}}$. The resulting system is solved to convergence with Newton’s method, as previously described for the CSA method.

2.4.1. Cyclic analysis: initial conditions

The computation of cyclic solutions of the airfoil problem requires the iterative process to be initialized with a starting solution. In general, the process does not converge when initial conditions are arbitrarily specified; the starting solution needs to reflect some degree of correct physical behavior. Time integrations of airfoil response in pitch and plunge revealed a clockwise rotation of the phase portrait in these two parameters (pitch plotted on the abscissa). An initial approximation to the LCO dynamics is imposed by assuming a circular trajectory in pitch and plunge (all other variables assumed to vanish), using the target cross-over value of plunge (β_2) to set the LCO amplitude. This starting solution is quite robust, and requires little knowledge of LCO period or the value of parameter λ .

Once one LCO solution is found with the CSA method for a specified amplitude, β_2 , then neighboring LCO solutions can be easily computed using the first solution (or closest solution) as an initial condition. Stochastic solutions are initialized as described above for \mathbf{X}_0 ; higher order terms are specified to vanish.

2.4.2. Cyclic analysis: expected value computation

The expected value of $f(\xi)$, $\langle f \rangle \equiv \frac{1}{2\pi} \int_{-\infty}^{\infty} f(\xi) e^{-\xi^2/2} d\xi$, can be evaluated with Gauss–Hermite quadrature, although for cyclic solutions, it is evaluated with a simpler, midpoint-rule integration. This approach is reasonable, given the following. First, computed LCO data are found to vary slowly with ξ over the range of interest, and second, only a small number of terms in the expansion (36) are required, thus diminishing the role of $\mathbf{H}\mathbf{e}(\xi)$ in increasing the order of variation. Usually, only the 1st-order term, $\widehat{\mathbf{X}}_1(\lambda_0)\mathbf{H}\mathbf{e}_1(\xi) = \widehat{\mathbf{X}}_1(\lambda_0)\xi$, is needed to capture adequately the probabilistic response.

The integration is carried out over a restricted range, $[\xi_{\min}, \xi_{\max}]$, instead of $\pm\infty$, since extreme values of $\gamma = k_3$ are very unlikely and either eliminate possible physical solutions (in the case of subcritical reduced velocities) or lead to spurious behavior of the CSA/CSP algorithms. The integration range is evenly subdivided into N_i intervals of width $\Delta\xi$, and the integral takes the form $\sum_{i=1}^{N_i} f_i e^{-\xi_i^2/2} \Delta\xi$, where each term is evaluated at interval midpoints.

2.5. Wiener–Haar time-domain analysis

To facilitate the use of the Haar wavelet, a transformation of the wavelet to a finite interval $\xi \in [a, b]$ is considered. Following [17], ζ , a uniform rv on $[0, 1]$, is defined whose realization is r . In a consistent manner, the realization of the random variable $\xi(\theta)$ associated with ζ is taken to be y . It is assumed that y and r are one-to-one. Then, the transformed wavelets $\{\Psi_k^{(j)}\}$ satisfy the orthonormality condition (with respect to the distribution of ξ)

$$\int_0^1 \psi_k^{(j)}(r)\psi_n^{(l)}(r) \, dr = \int_a^b \Psi_k^{(j)}(y)\Psi_n^{(l)}(y) \, dM_\xi(y) = \delta_{j,l}\delta_{k,n}. \tag{41}$$

Applying (41) to (29), the WHa expansion takes the following form for a time-dependent, random process, $x_i(t, \xi)$ (N such processes are considered to participate in (1):

$$x_i(t, \xi(\theta)) = [x_i]_0(t) + \sum_{j=0}^{\infty} \sum_{k=0}^{2^j-1} d_k^{(j)} \Psi_k^{(j)}(\xi(\theta)), \tag{42}$$

$$= [x_i]_0(t) + \sum_{j=0}^{\infty} \sum_{k=0}^{2^j-1} d_k^{(j)} \psi_k^{(j)}(Pr(\xi)), \tag{43}$$

where $[x_i]_0(t) = \langle x_i(t, \xi) \rangle$ (the expected value is defined in (14)).

In practice, the series (43) is truncated to some resolution level $j = J$, and x_i is regarded to be the i th component of an array of values, each discrete in time, whose index here is designated by a superscript n . Then, (43) becomes

$$x_i^n(\xi) \approx [x_i^n]_0 + \sum_{j=0}^J \sum_{k=0}^{2^j-1} d_k^{(j)} \psi_k^{(j)}(Pr(\xi)). \tag{44}$$

The wavelet coefficients are (the dependence on i and n are removed here to preserve notational simplicity)

$$d_k^{(j)} = \int_0^1 x_i^n(M_\xi^{-1}(r))\psi_k^{(j)}(r) \, dr, \tag{45}$$

and take the convenient form $d_k^{(j)} = \langle x_i^n \psi_k^{(j)} \rangle$ if ξ is uniformly distributed (i.e., $\xi = \zeta$).

Mallat’s algorithm for the discrete wavelet transform (DWT) is employed to compute the 2^{J+1} WHa expansion coefficients [22]. This approach is very computationally efficient, converging much faster than MCS. Details are given in [32].

2.6. B-spline-based stochastic projections

In the preceding formulation of the cyclic methodology, the assumed spectral representation of the response behavior is infinitely differentiable. Yet, in modeling subcritical bifurcation behavior, the desired responses do not carry this smoothness: at critical values of the initial angle of attack, for example, there is a jump in the response, where the large-time aeroelastic solution transitions from equilibrium to LCO. This behavior is shown in Fig. 8 for the case described in more detail in Section 3.

The stochastic projections can be treated, however, as piecewise continuous over the interval of interest. Following Millman et al. [26], splines can be used to approximate these kinds of projections. An important property of the multivariate B-splines they choose is that the splines are a compact support basis; i.e., the influence of any particular B-spline coefficient extends over a few intervals [7]. The practical significance of this property is that oscillations in the vicinity of discontinuous behavior can be avoided with the proper choice in the order of the B-spline. The order used in this work is $k_{\xi_1} = k_{\xi_2} = 2$, which is equivalent to a piecewise linear interpolation [7]. Their multivariate B-spline is

$$\alpha(\xi_1, \xi_2) = \sum_{i=1}^{N_{\xi_1}} \sum_{j=1}^{N_{\xi_2}} \hat{\alpha}_{ij} B_{j,k_{\xi_2},z_{\xi_2}}(\xi_2) B_{i,k_{\xi_1},z_{\xi_1}}(\xi_1), \tag{46}$$

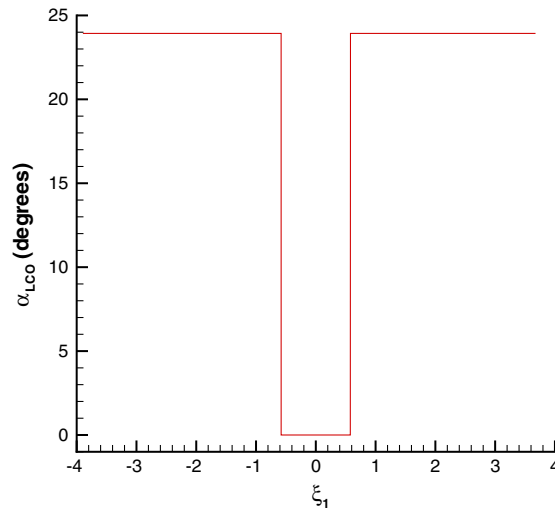


Fig. 8. Variation of peak angle of attack attained during LCO at $\lambda = 6.2$ as a function of the normal random variable corresponding to initial angle of attack (ξ_1) following [26].

where \mathbf{z}_{ξ_1} is the vector of N_{ξ_1} knots on the ξ_1 axis (associated with initial pitch angle) and \mathbf{z}_{ξ_2} is the vector of N_{ξ_2} knots on the ξ_2 axis (associated with cubic stiffness).

The details of the stochastic projection based on B-splines are now given, using the presentation of Millman [27]. In general terms, a sub-domain is first chosen in the stochastic (ξ_1, ξ_2)-domain over which samples of the LCO amplitude will be obtained. Next, the location of nodes to be sampled in that interval is determined. The multivariate B-spline that approximates the response surface in the stochastic domain is then determined. Finally, an MCS is performed on this response surface to estimate the PDF of the response. Each of the steps of this algorithm is now described in detail.

The sub-domain selected is based on the distribution of random variables. For the airfoil problem the rvs are assumed to be standard normal. Strictly speaking, the domain defined for a Gaussian rv is the whole real line. There is, however, a practical limit to this interval: the parameters associated with rvs must be kept within specified bounds in order for the equations of motion to be sensible and numerically well behaved. In the B-spline results reported below, for which the standard deviations of the physical parameters are assumed to be fairly large, the corresponding rvs are confined to values within $[-4, 4]$. This sub-domain captures 99.99% of the possible responses [26].

Nodes within the two-dimensional sub-domain are prescribed using a Gaussian distribution to obtain intervals distributed at equivalent increments of probability [26]. Symmetry is also imposed on the distribution between the two rvs. To achieve closure, nodes are placed at the end points of the subdomain and at $\xi = \pm 2.5$ for both rvs to provide a certain level of smoothness in matching the interior Gaussian distribution to the end-point values. Assuming that I represents the number of nodes distributed in each of the two coordinate directions, Table 1 gives the positions of the nodes within the sub-domain. Samples of the response are obtained at the selected values of ξ_1 and ξ_2 .

From these samples, the multivariate B-spline problem can be solved for the coefficient matrix, $\hat{\alpha}_{ij}$ in (46), the details of which are given in [7]. After these coefficients are determined, an MCS is performed in (46), which is extremely efficient, since the response properties of the aeroelastic model are already encoded in the spline coefficients.

Before proceeding to the next section, it is noted that B-spline algorithm fits well into the stochastic projection framework developed elsewhere. Consider the array of nodes \mathbf{z} such that $z_i \in [-a, a]$ and $z_1 = -a < z_2 < \dots < z_I = a$ for some integer I and some cutoff value a (4 above). Since it was noted that the above algorithm is a piecewise linear interpolation, the appropriate basis for expansion would be the hat function, which has the property [7]

$$\Psi_j(z_i) = \delta_{ij}, \quad (47)$$

Table 1
Gaussian distributed nodes (symmetric in ξ)

| $I = 6$ | $I = 10$ | $I = 18$ |
|----------|----------|----------|
| – | – | ±0.15731 |
| – | ±0.31864 | ±0.31684 |
| – | – | ±0.48878 |
| ±0.67449 | ±0.67449 | ±0.67449 |
| – | – | ±0.88715 |
| – | ±1.15035 | ±1.15035 |
| – | – | ±1.53412 |
| ±2.5 | ±2.5 | ±2.5 |
| ±4.0 | ±4.0 | ±4.0 |

where δ_{ij} is the Dirac delta function. Thus

$$\Psi_j(z_i) = \begin{cases} 1, & i = j, \\ 0, & i \neq j. \end{cases} \tag{48}$$

Also notice that $\delta_f(z) = \delta(z - z_j)$, which indicates sampling at a node. Then inner products, with unit weight functions, are given as

$$\langle \Psi_i, \delta_j \rangle = \int_{-a}^a \Psi_i(z) \delta(z - z_j) dz = \Psi_i(z_j) = \delta_{ij}, \tag{49}$$

$$\langle z \Psi_i, \delta_j \rangle = \int_{-a}^a z \Psi_i(z) \delta(z - z_j) dz = z_j \Psi_i(z_j) = z_j \delta_{ij}. \tag{50}$$

Restricting attention, for convenience, to one rv, the piecewise linear approximation to the response $\alpha(t, \xi)$ becomes

$$\alpha(t, \xi) = \sum_{i=1}^I \hat{\alpha}_i(t) \Psi_i(\xi). \tag{51}$$

Thus, the samples of the random variable are used to obtain samples of the response and a piecewise linear approximation to the response is obtained from the B-splines. While the WHe expansion provides a best fit to the stochastic projection and converges, in the mean square sense to an MCS [13], the piecewise linear interpolation is exact at the nodes and converges exactly to the MCS when the number of nodes equals the number of samples obtained by the MCS.

3. Results

Results of the stochastic airfoil analysis are now reported for the Cyclic, Haar wavelet, and B-spline techniques. Two basic airfoil configurations are considered: a softening torsional structure, defined deterministically by $k_3 = -3$ and $k_5 = 20$, that leads to a subcritical Hopf bifurcation, and a hardening structure, defined by $k_3 = 3$ and $k_5 = 20$, that leads to a supercritical Hopf bifurcation [29]. In both cases, the bifurcation takes place at $\lambda^* \approx 6.285$. In this paper, attention is primarily given to the problem of subcritical bifurcations, owing to the greater challenge posed by the existence of multiple LCO states over a range of λ values.

Owing to the nature of this survey, results are collected with different methods, each referred to differently. To avoid confusion, the relevant acronyms are reviewed before proceeding.

- CSA Cyclic analysis for a specified amplitude value
- CSP Cyclic analysis for a specified parameter value
- ISCSP Intrusive stochastic analysis with CSP
- PSCSP Non-intrusive stochastic analysis with CSP
- WHa Wiener–Haar expansion of data
- WHe Wiener–Hermite expansion of data

In the stochastic analysis, variability in k_3 and initial pitch angle, $\alpha_0 \equiv \alpha(0)$ is considered, assuming the following Gaussian characteristics:

$$k_3(\xi) = [k_3]_0 + [k_3]_1 \xi, \quad (52)$$

$$\alpha_0(\xi) = [\alpha_0]_0 + [\alpha_0]_1 \xi, \quad (53)$$

where $[k_3]_0$ is set to match the deterministic value (± 3). Results of cyclic analysis are limited to variability in spring stiffness, while the non-intrusive B-spline technique accounts for variability in k_3 and α (the ability of non-intrusive techniques to treat multiple random variables should be considered an advantage of the approach). Following results reported in [2,26], cyclic solutions are obtained for $[k_3]_1 = 0.2$ and B-spline stochastic projections are computed with $[k_3]_1 = 0.3$. While the difference in the value of $[k_3]_1$ assumed in the two studies influences the range over which data is sampled, once the coefficients $\hat{\mathbf{X}}_i$ (cyclic) and $\hat{\alpha}_i$ (B-spline) are computed, simulated realizations are obtained with either method using essentially the same approach. For the B-spline method, which is sensitive to α_0 , the following are assumed: $[\alpha_0]_0 = 0^\circ$ and $[\alpha_0]_1 = 0.2$ rad. Lastly, plunge values are reported in nondimensional form, using airfoil chord as a scale factor.

Following the notation of Lee et al. [16] the following values of aeroelastic parameters are specified: $\mu_s = 100$, $a_h = -0.5$, $x_\alpha = 0.25$, $\omega_r = 0.2$, $\gamma_\alpha = 20$, and $r_\alpha = -0.5$. All methods used a time discretization that rendered the results insensitive to further time-step refinement. Generally, as LCO amplitude (β_2) decreases, less resolution in the time step is required to capture the LCO accurately.

Results are presented in the following order. First, the character of LCOs at different points along the solution surface emanating from the bifurcation point is examined, and then the dependence on the initial angle of attack considered. Next, stochastic LCO modes are obtained at selected points, and their relative size used to assess the convergence properties of the Hermite expansion, as well as potential numerical differences brought about by employing either an intrusive or non-intrusive formulation. Finally, probability of failure is estimated for the aeroelastic system over a range of flight speeds.

3.1. Assessment of available LCOs

For a subcritical bifurcation ($k_3 = -3$), LCOs are computed with the CSP method at two reduced velocities: $\lambda = 6.5$ and $\lambda = 6.2$. In the latter case, two LCO solutions are available between λ^* (≈ 6.285) and λ^{LCO} (≈ 5.908); a single LCO is computed for $\lambda = 6.5$. Starting from these three points, new LCO states are computed at different reduced velocities, in increments of $\Delta\lambda = \pm 0.01$. Through this continuation process, a solution diagram, like that given above, is now revealed. See Fig. 9(a). Using the pitch and plunge variables, a phase-plane representation of each LCO is shown in Fig. 9(b). In this figure it is seen that the LCOs on the upper branch (i.e., amplitudes larger than at λ^{LCO}) are quite similar, while the LCO on the lower branch (i.e., amplitudes smaller than at λ^{LCO}) is of smaller magnitude and characterized by smoother behavior at values of peak pitch angle. It should also be noted that the CSA method enables a single process of continuation to compute both stable and unstable LCOs. In contrast, continuation with the CSP method fails when λ is reduced below λ^{LCO} ; i.e., the method cannot “turn” the limit point. Thus, the CSP method requires two starting solutions, one for each branch.

3.2. Stochastic analysis with the cyclic methods

Results are now presented for stochastic analysis of LCOs using the cyclic methods. The analysis is localized around points of interest, including points corresponding to speeds above and below λ^* . Intrusive and non-intrusive methods are compared in terms of the numerical results.

3.2.1. The PSCSP method

As described above, application of the CSP method to an ensemble of cases at regularly spaced values of ξ (i.e., cubic stiffness) yields data used to compute the PCE coefficients of \mathbf{X} . This technique is referred to as PSCSP and is applied here to examine the expansions at the same two reduced velocities considered above:

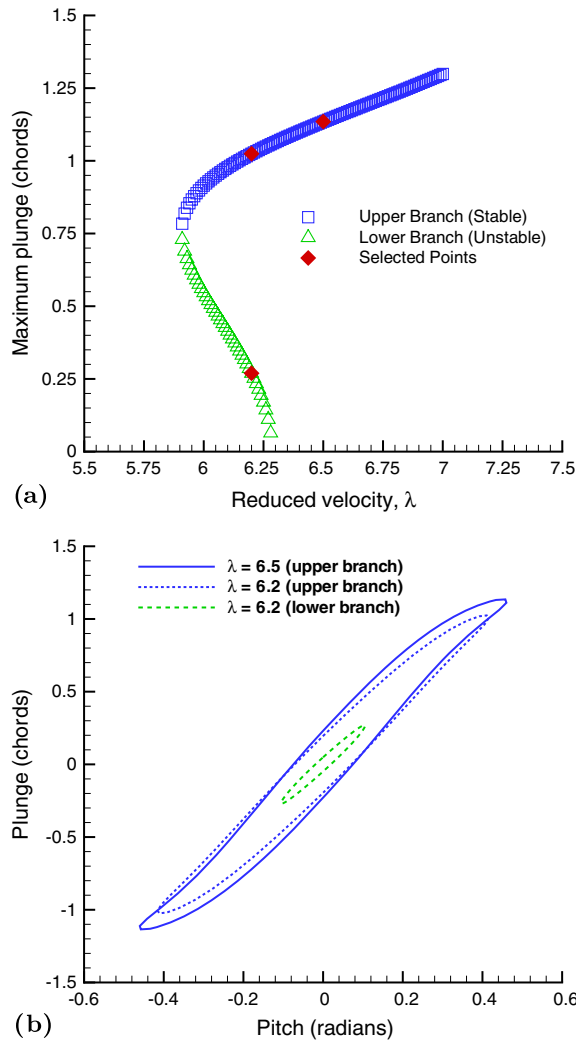


Fig. 9. Application of the CSP method: (a) stable and unstable LCO branches, along with selected LCOs at $\lambda = 6.5$ and $\lambda = 6.2$; (b) phase plane representations of stable and unstable LCOs at selected points.

$\lambda = 6.5$ (supercritical) and $\lambda = 6.2$ (subcritical). The character of all solutions is assessed in terms of the cyclic behaviors of the expansion coefficients, $\widehat{\mathbf{X}}_i$, in terms of pitch and plunge.

In the expected value computation of \mathbf{XHe}_i (cf. (39)), an integration range of $\xi_{\min} = -5$ to $\xi_{\max} = 5$ includes all but a few, least likely, spring-stiffness values (in the tails of the Gaussian distribution), and guarantees convergence of the CSP method for the interesting values of λ selected above. As might be expected, the availability of subcritical LCO solutions is somewhat sensitive to $\gamma = k_3$. Branches of LCO solutions for the extreme values of $\gamma = k_3$ (the endpoints of the integration range for the expected value) are shown in Fig. 10(a), where substantial movement in the location of the cyclic fold is evident. The fold is located at about $\lambda = 5.6$ for the spring with the most nonlinear softening ($k_3 = -4$), and at about $\lambda = 6.12$ for the spring with the least nonlinear softening ($k_3 = -2$). Thus, when $\lambda = 6.1$, a 5σ -variation of k_3 cannot be fully explored, since for the largest values of k_3 , solutions would not be available.

It is reasonable to question the applicability of Gaussian distributions for parameters of interest in LCO, since without compact support, there is an expectation that rare realizations of parameter values are not physically realizable. This problem is numerically confined in the cyclic procedures by selecting the ranges over which ξ should reasonably vary. However, this approach is ad hoc and should be replaced by a more robust

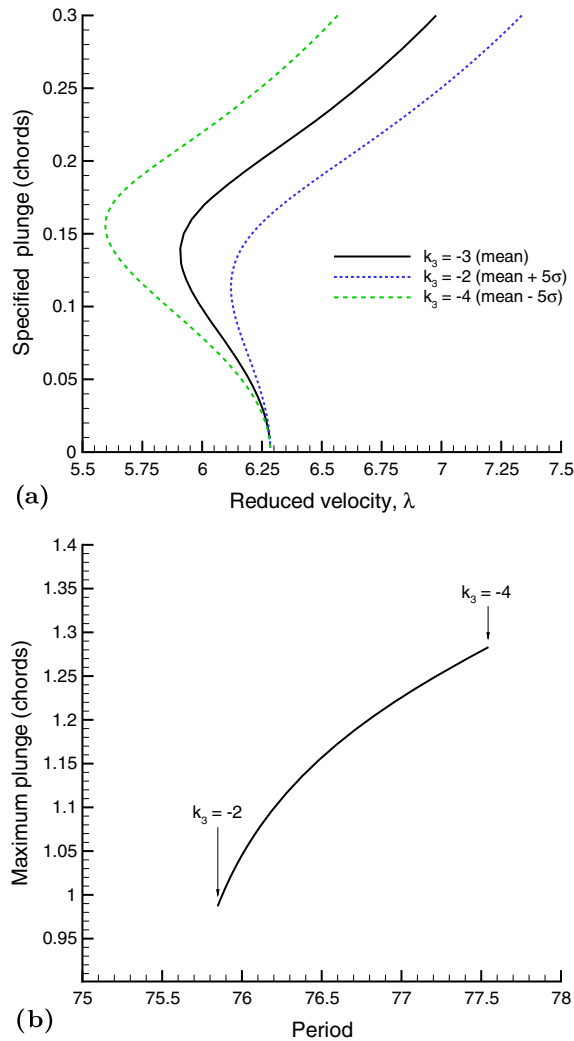


Fig. 10. LCO sensitivity to cubic stiffness (k_3): (a) different LCO branches (in terms of specified amplitude, β_3) for 5σ variations of k_3 ; (b) variation of maximum plunge as a function of k_3 at $\lambda = 6.5$ (in terms of LCO period, T).

procedure that will give the analyst greater control over the stochastic analysis. Such a procedure is embodied in the WHa expansions, to be discussed later. For this local basis, compact support is provided, and the capacity to jump from a state of LCO to no LCO at a critical value of the parameter exists [17]. The use of Hermite expansions in the cyclic methodology here serves to demonstrate the ability of the non-time-domain approach to capture the stochasticity of LCOs (in a manner that is highly convergent, as to be described shortly). While not currently available, the cyclic framework can be extended to incorporate decomposition of the stochastic dimension with, for example, the Haar wavelet.

While the availability of solutions can restrict the appropriate range of spring-stiffness variations using Hermite polynomial expansions, the variation of LCO characteristics within this range is quite smooth. For example, the dependence of LCO amplitude on k_3 (in terms of maximum plunge) over the range of values considered above is shown in Fig. 10(b). There it is seen that a very low-order polynomial would be adequate in describing the variation. In general, this observation is applicable to all the components of \mathbf{X} , which suggests that only a small number of terms in the expansion are required.

The efficiency of the expansion is verified through inspection of the computed expansion coefficients. First, the pitch and plunge components of $\hat{\mathbf{X}}_i$ are viewed for $\lambda = 6.5$. Two different values of N_i (the number of inter-

vals in the expected value integration) are considered, $N_i = 10$ and $N_i = 100$, to show convergence in the probability dimension. Four coefficients are considered, $\hat{\mathbf{X}}_0$ through $\hat{\mathbf{X}}_3$, and these are shown in Fig. 11. The 0th-order term is found to be in very close agreement with the deterministic LCO solution computed at $k_3 = -3$ (the mean value in the PSCSP analysis), with some level of physical nonlinearity at the largest values of pitch and plunge evident in the cycle. PSCSP predictions for both values of N_i are nearly in exact agreement. At 1st-order, a somewhat greater degree of nonlinearity in the cycle is seen, and again, there is almost no sensitivity to N_i . At 2nd-order, the pitch/plunge cycle is deformed into a “figure-eight,” and very slight differences become apparent between the predictions between the two values of N_i . This is to be expected, since as the order of the term increases, so does the variability of $\text{He}_i(\xi)$, which starts to degrade the accuracy of the expected value computations. However, it should be noted that at 2nd-order, the magnitude of the coefficients are nearly four orders of magnitude smaller than that of the 0th-order term, and two orders of magnitude smaller than that of the 1st-order term, which shows the relative insignificance of the higher order contribution to the general behavior of the system. The trends are continued at 3rd-order: smaller amplitudes, heightened cyclic nonlinearity, and somewhat greater sensitivity to N_i (but differences still small).

Attention is now turned to the behavior of the PCE coefficients for the subcritical case of $\lambda = 6.2$. These results are presented in Fig. 12 for both the stable and unstable LCO at this reduced velocity, although the issue of sensitivity to N_i is documented for the unstable LCO, which is most dissimilar to what was just shown

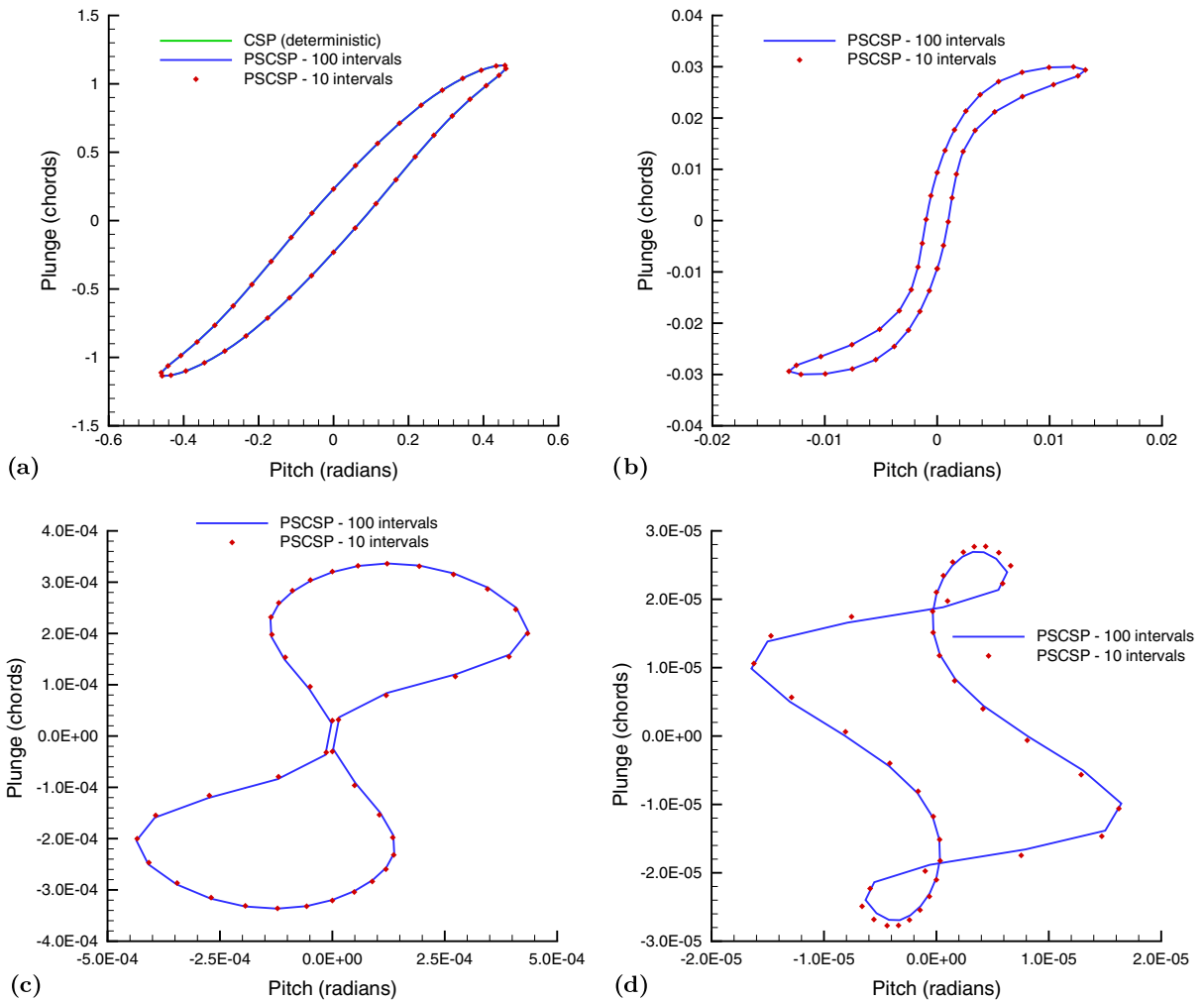


Fig. 11. Comparison of PSCSP predictions of $\hat{\mathbf{X}}_i$ components (pitch and plunge) during LCO at $\lambda = 6.5$ for two different numbers of intervals, N_i : (a) $\hat{\mathbf{X}}_0$ (includes the deterministic CSP prediction for comparison); (b) $\hat{\mathbf{X}}_1$; (c) $\hat{\mathbf{X}}_2$; (d) $\hat{\mathbf{X}}_3$.

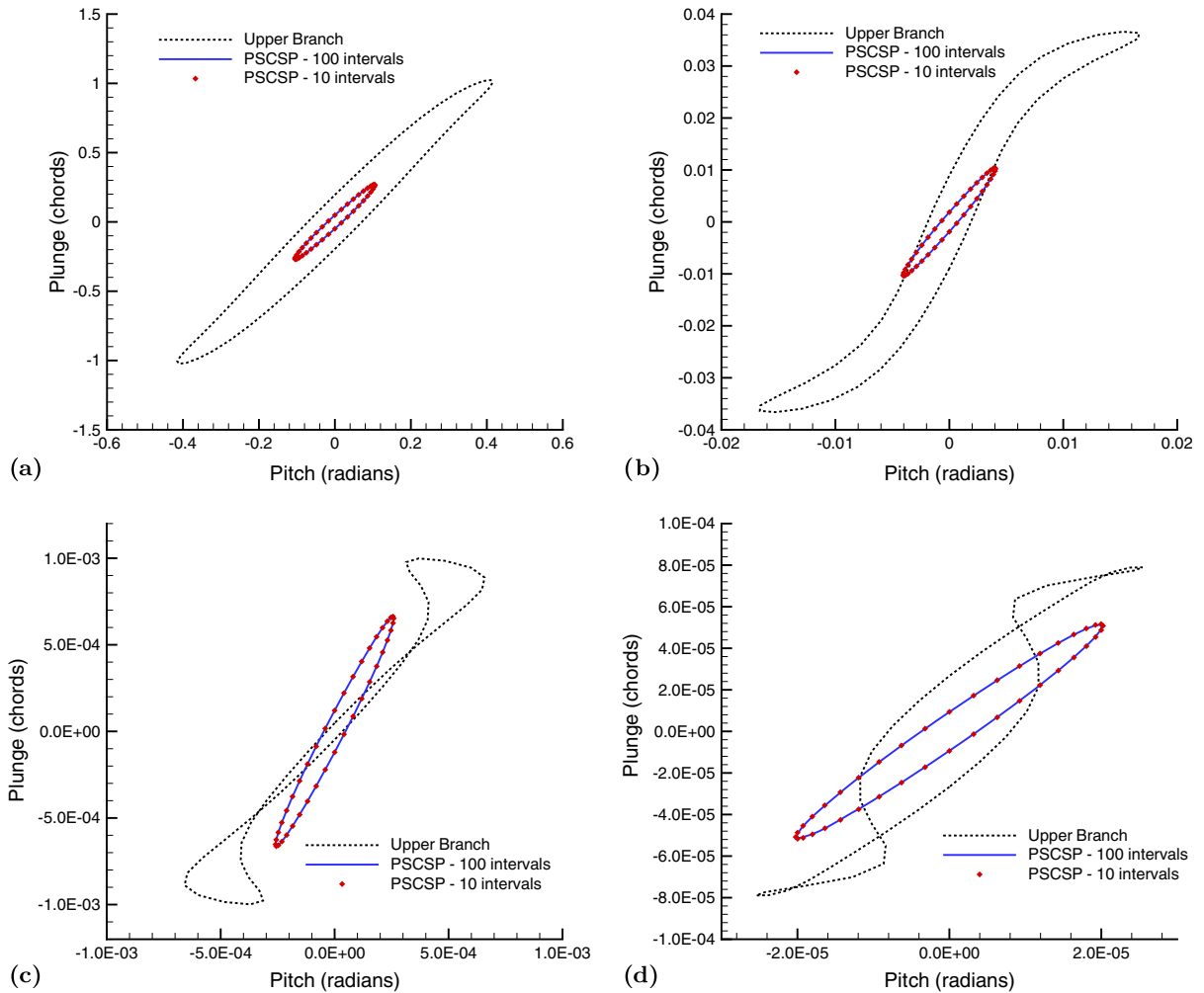


Fig. 12. Comparison of PSCSP predictions of \hat{X}_i components (pitch and plunge) during LCO at $\lambda = 6.2$ (lower branch) for two different numbers of intervals, N_i : (a) \hat{X}_0 ; (b) \hat{X}_1 ; (c) \hat{X}_2 ; (d) \hat{X}_3 . PSCSP predictions of \hat{X}_i on the upper branch are included for comparison ($N_i = 10$).

for $\lambda = 6.5$. Not surprisingly, the behavior of the WHe expansion coefficients for the large-amplitude, stable LCO (upper branch) is seen to be similar to that just reviewed. Curiously, though, the coefficients associated with the unstable LCO (lower branch) do not show an increasing level of physical nonlinearity as the order of the term increases. Also, while the coefficient amplitudes are generally smaller than for the stable LCO, the 2nd- and 3rd-order coefficients of the unstable LCO grow to nearly the amplitude of that of the stable LCO. Furthermore, the amplitude of both coefficients is more than a factor of two larger than for $\lambda = 6.5$. It may be speculated that these changes in amplitude are attributable to the proximity of λ to the cyclic fold, particularly when k_3 is largest, when there are relatively larger variations in LCO amplitude than at supercritical values of λ (owing to the change in slope of the solution path near the fold). However, this point should be further investigated. Still, these effects are evident only in the higher order terms, which are more than an order of magnitude smaller than the 1st-order term.

3.2.2. The ISCSP method

Results computed with the ISCSP method at $\lambda = 6.5$ and $\lambda = 6.2$ (unstable solution on lower branch) are now compared with that obtained using the PSCSP approach. In all cases, $N_i = 10$ is assumed. When describing the ISCSP results, the phrase “ N th-order” denotes the order of the WHe expansion used in the analysis.

Thus, a 1st-order ISCSP analysis involves only a two-term expansion, and leads to predictions of $\widehat{\mathbf{X}}_1$ that are, in general, different than what would be predicted with a 2nd-order analysis. The differences are caused by nonlinear couplings between expansion terms appearing at different orders in the intrusive formulation. This stands in contrast with the PSCSP approach, where the coefficient calculation at one order is independent of the calculation at another order (i.e., the calculations are based solely on the ensemble data).

Excellent agreement between the PSCSP and ISCSP methods is observed. The expansion coefficients are shown in Fig. 13, in terms of pitch and plunge, for cases of greatest interest. First, the 1st-, 2nd- and 3rd-order coefficients are reported in Figs. 13(a)–(c) for $\lambda = 6.5$. In Fig. 13(a), the analysis with the ISCSP method is applied at two different orders, and found to yield results nearly equivalent to that of the PSCSP method. Calculation of $\widehat{\mathbf{X}}_2$ shows a slight improvement by going to 3rd-order in the ISCSP analysis, at which point the results become nearly identical to that of the PSCSP method. Again, for $\widehat{\mathbf{X}}_3$ computed results are in excellent agreement. Finally, in Fig. 13(d), the 3rd-order component of the LCO (lower branch) at $\lambda = 6.2$ is examined. For this more benign LCO, the ISCSP and PSCSP methods provide results that are indistinguishable.

The purpose of the ISCSP method is to provide an efficient means for computing the stochasticity of LCOs by replacing a large number of deterministic calculations from which variability is observed (i.e., sampling) with a single calculation in which uncertainties are propagated through the analysis. However, the PSCSP

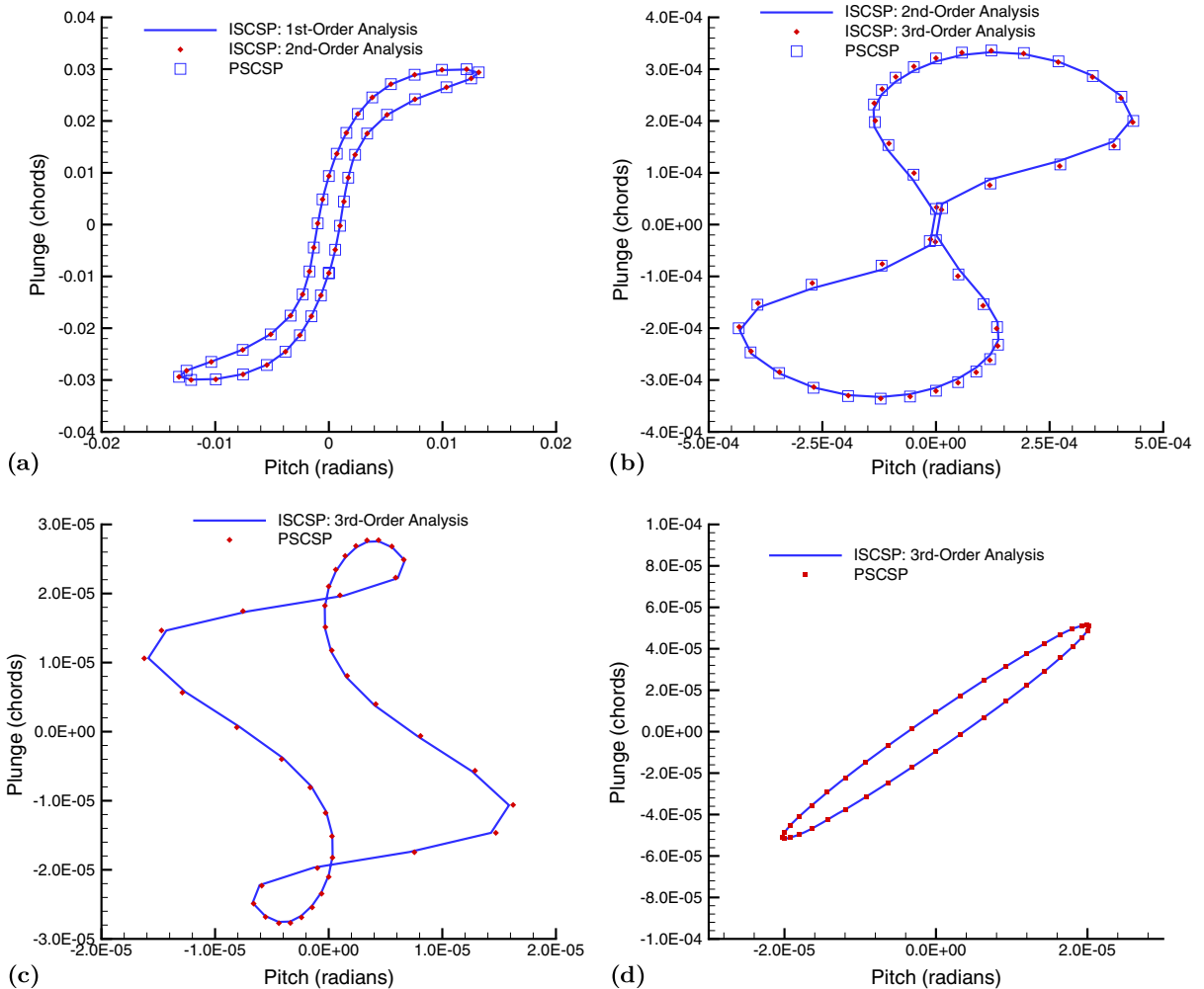


Fig. 13. Comparison of ISCSP and PSCSP predictions ($N_i = 10$) of $\widehat{\mathbf{X}}_i$ components (pitch and plunge) during LCO at $\lambda = 6.5$ and $\lambda = 6.2$ (lower branch): (a) $\widehat{\mathbf{X}}_1$ and $\lambda = 6.5$; (b) $\widehat{\mathbf{X}}_2$ and $\lambda = 6.5$; (c) $\widehat{\mathbf{X}}_3$ and $\lambda = 6.5$; (d) $\widehat{\mathbf{X}}_3$ and $\lambda = 6.2$.

method is found to be much more efficient than the currently implemented ISCSP method, since relatively few full-order realizations are needed to compute the WHe expansion coefficients with the PSCSP approach. The Jacobian in the ISCSP methodology is numerically evaluated and of larger size than that of the PSCSP (or CSP) approach. Thus, the current ISCSP formulation involves additional function evaluations, each requiring expected value computations like that used in the PSCSP technique. It is possible that the ISCSP method could become more competitive with the PSCSP method if the evaluation of the expected values, $\langle GHe_i \rangle$, could be analytically accelerated, but this possibility is unlikely for more complicated analysis using computational fluid dynamics. Still, both methods are faster than a straightforward sampling-based approach, like Monte-Carlo simulation.

3.2.3. Validation of the stochastic cyclic analysis

The stochastic analysis (PSCSP and ISCSP methods) is validated by comparing simulated realizations \mathbf{X} , as a function of $k_3(\xi)$ over the interval $\xi_{\min} = -5$ to $\xi_{\max} = 5$, to actual realizations computed with the CSP method. The reduced velocity (λ) is specified to be 6.5. The simulated realizations are evaluated by substituting computed WHe expansion coefficients into (36). The level of agreement between the stochastic projection methods and the full-order simulations was excellent.

Comparisons between the stochastic methods and the CSP technique are provided in Fig. 14. The comparison is achieved by examining predicted maximum plunge of the LCO, as extracted from \mathbf{X} , at 10 values of k_3 evenly distributed over the range of ξ examined. An L2-norm of the difference between the predictions of the CSP method and either stochastic method ($\|\Delta\mathbf{X}\|_2$) is also calculated. In computing the stochastic results, N_i is assumed, and the ISCSP calculations are carried out to 3rd-order in the PCE. Using the WHe expansion coefficients that are determined, lower orders of coefficients are retained to examine the dependence of the difference norm on the number of terms included in the expansion.

As desired, both the PSCSP and ISCSP methods yield near equivalent results over equivalent expansion orders. Results for the PSCSP method are shown in Fig. 14(a). In this figure, which includes an inset giving greater detail of the solutions near ξ_{\max} , it is evident that increasing order of the PCE improves the comparison through third order. This observation is confirmed by evaluating $\|h_{\text{CSP}}^p - h_{\text{PSCSP}}^p\|_2$, where h_{CSP}^p and h_{PSCSP}^p are maximum values of plunge predicted by the CSP and PSCSP methods over the permitted range of ξ values. Norm values at various orders are 0.00288 (1st order), 0.00279 (2nd order), 0.000617 (3rd order), and 0.00313 (7th order). When order is increased to 7th order, the PSCSP results obviously diverge from the CSP results. This behavior warrants further investigation, but may be attributable to the need for increasing the range of k_3 over which full-order realizations are gathered in the PSCSP computations, or numerical sensitivities arising from the admission of higher order terms in the assumed expansions beyond that which is reasonably sup-

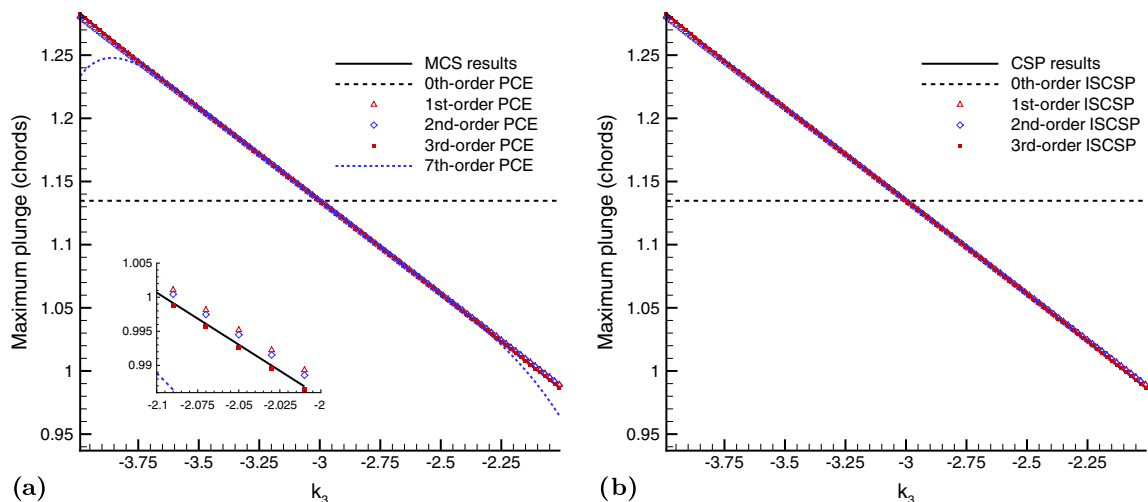


Fig. 14. Comparison of maximum plunge values during LCO computed with deterministic (CSP) and stochastic analysis over complete range of spring stiffness variations: (a) PSCSP results; (b) ISCSP results.

ported by the data. Similar trends in the accuracy of the ISCSP are exhibited through 3rd order, where the norms are 0.00288 (1st order), 0.00277 (2nd order), and 0.000520 (3rd order). Higher orders were not investigated.

3.3. Time-domain analysis with WHa expansions

While the WHe expansion works well when applied to the LCO data presented in cyclic form, where the time domain in a sense is restricted, it is seen above that expansion fails in the physical time domain. The root of the problem is in the inadequacy of the WHe expansion to capture the growing nonlinearity of the response with respect to the rv with increasing time. A multi-resolution analysis is now employed to provide improved resolution, even for large times.

WHa expansions are computed for the low-order airfoil problem assuming variability only in k_3 . This parameter is expressed as a function of ξ , which is assumed to be a uniform rv [32], in a manner consistent with the formulation presented above for \mathbf{x} , and the derivation of WHa coefficients through the discrete wavelet transform.

It is first demonstrated that the WHa expansion does an excellent job of resolving the extreme nonlinearity of $\alpha(t, \xi)$ at large time. Results are shown for the case of spring hardening (supercritical LCO at $\lambda = 6.5$) and softening (subcritical LCO at a point very close to λ^* , $\lambda = 6.284$) in Fig. 15 for $t = 18,000$, a time sufficiently large for the WHe expansion to collapse. When the spring either hardens or softens, Fig. 15 shows rapid variation of α with respect to realizations of ξ less than about 0.4; for these realizations, LCO has developed at times much less than 18,000. The variation of oscillation frequency with stiffness, accumulated over numerous oscillations, is the mechanism for the rapid changes in α . In the case of spring hardening, when realizations of ξ are sufficiently large, LCO amplitude is diminished as the nonlinearity becomes sufficiently strong. For spring softening, realizations in ξ above 0.4 eliminate LCO altogether, since the corresponding increase in k_3 from its deterministic value of -3 restricts the subcritical behavior of the system. Also shown in Fig. 15 is the improvement in the WHa prediction of the deterministic behavior (the “full model”) when the resolution level is increased from $J = 6$ to $J = 7$. At this level, the nonlinear variations in α are very closely reproduced.

Focusing attention now on the density functions of the airfoil response, once in LCO, it is found that the WHa expansion successfully reproduces the stochastic characteristics of the deterministic system, as obtained through a 4000-sample Monte-Carlo simulation. In Fig. 16 it is seen that the WHa expansion converges rapidly, matching very closely the sampling results of the deterministic system at resolution level $J = 8$ (512 expansion coefficients).

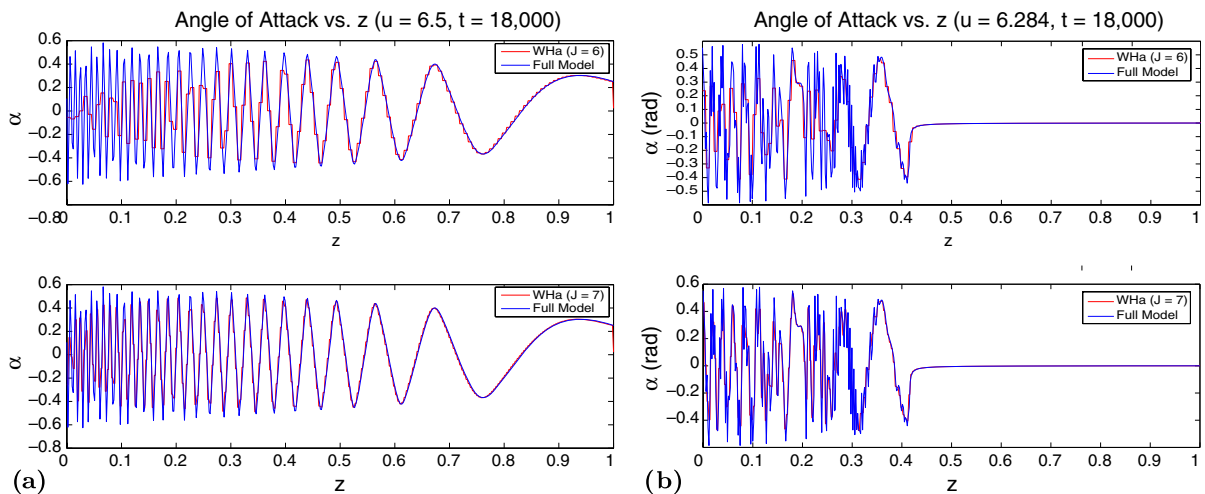


Fig. 15. Variation of pitch angle (radians) with respect to realizations of ξ (here designated as z) for: (a) spring hardening ($\lambda = 6.5$), and (b) softening ($\lambda = 6.284$).

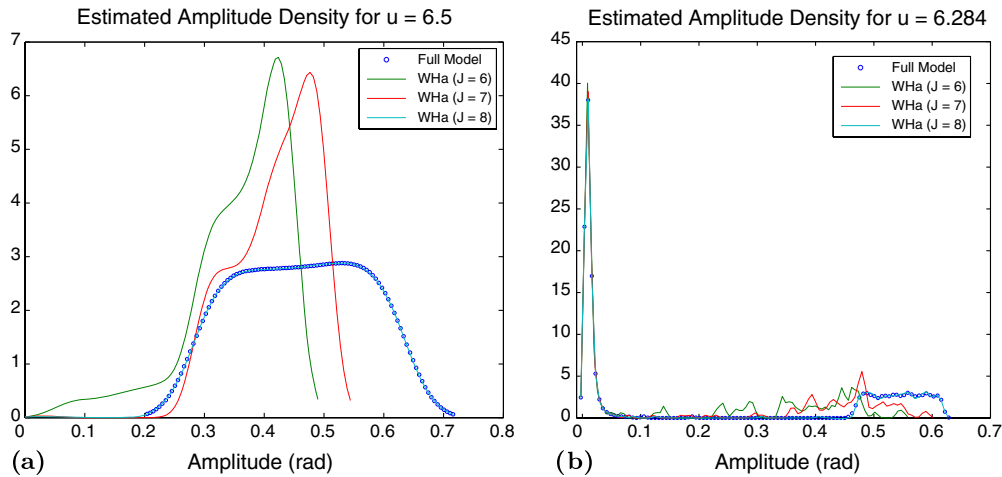


Fig. 16. Convergence of LCO amplitudes for: (a) spring hardening ($\lambda = 6.5$), and (b) softening ($\lambda = 6.284$). Each plot shows a kernel-based estimator of the density function for each of three WHa resolution levels.

3.4. Fast predictions of failure probability with B-splines

Fast predictions of failure probability are obtained using B-spline stochastic projections of sampled LCOs [27]. Results, which will appear elsewhere, will be reviewed here in two sets. First, stochastic LCO responses are shown for the cases of spring hardening and softening described above, assuming the low-order airfoil model. These results are shown to further demonstrate the bi-modal character of response distributions in the presence of subcritical bifurcations. Then, the efficacy of the B-spline approach is demonstrated for LCO results obtained using a higher order model based on computational fluid dynamics (CFD). The parameters considered to be uncertain are k_3 (ξ_2) and α_0 (ξ_1): their distributions are Gaussian as described at the start of Section 3.

3.4.1. Low-order airfoil model

Compact representations of LCO behavior, as represented by peak pitch angle (designated α_{LCO}), are computed through the B-spline-based stochastic representation (46) using sampling of LCO response at selected nodes. Nodes are sampled, as described in the Formulation section, at key locations within a square domain of parameter values for which extreme values of $|\xi_1|$ and $|\xi_2|$ do not exceed 4, and the corresponding samples are used to compute the coefficients $\hat{\alpha}_{ij}$. Once the coefficients are found, then a fast MCS of (46) is carried out at different flight speeds to predict the probability that an LCO is encountered (for the spring softening case).

The number of nodes needed to derive accurate stochastic models depends on the nature of the spring response. For the case of spring hardening, response variations with respect to changes in structural stiffness are smooth, and there is no variation with respect to initial angle. A symmetric array of 36 nodes, 6 in the ξ_1 stochastic coordinate direction and 6 in the ξ_2 direction were found to be sufficient. In contrast, the case of spring softening was more demanding. For this problem, a discontinuity in the variation of the response with respect to α_0 is encountered (cf. Fig. 8). Capture of the geometric properties of the discontinuous surface in the $\xi_1 - \xi_2$ sub-domain required an increased number of nodes: 10 in the ξ_2 direction and 18 in the ξ_1 direction. Clearly, when the nodes are spaced according to Table 1, the surface is not captured perfectly. To assess the convergence of the scheme when a discontinuity is present, 6 nodes and 10 nodes are retained in the ξ_1 direction, and the MCS results compared to that of the 180-node model.

For evaluation, PDFs of LCO response predicted by the B-spline technique are computed for the case of spring hardening at $\lambda = 6.5$ and the case of spring softening at $\lambda = 6.2$. The results, which are shown in Fig. 17, are assessed by comparing an MCS of the deterministic model to that of an MCS based on (46) (4000 samples

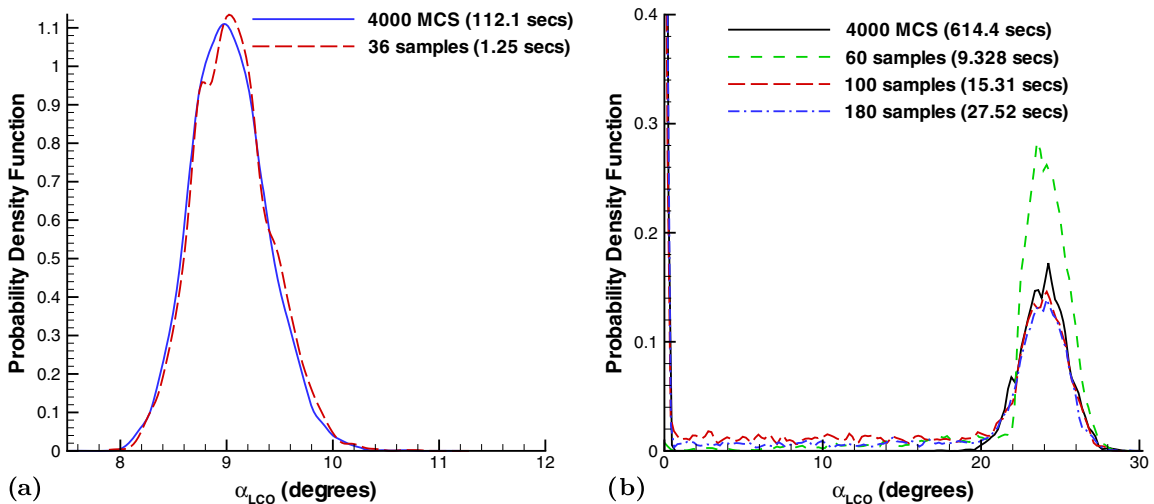


Fig. 17. Comparison of PDFs of LCO response computed with MCS for both deterministic and B-spline models: (a) spring hardening ($\lambda = 6.5$), and (b) spring softening ($\lambda = 6.2$). Computational time annotated.

each). It is found that for spring hardening, 36 samples of LCO behavior are sufficient to capture the response PDF well over the range the ξ values considered. Owing to the relatively low number of samples needed to describe the system for this case, the B-spline technique is found to accelerate MCS by nearly a factor of 100.

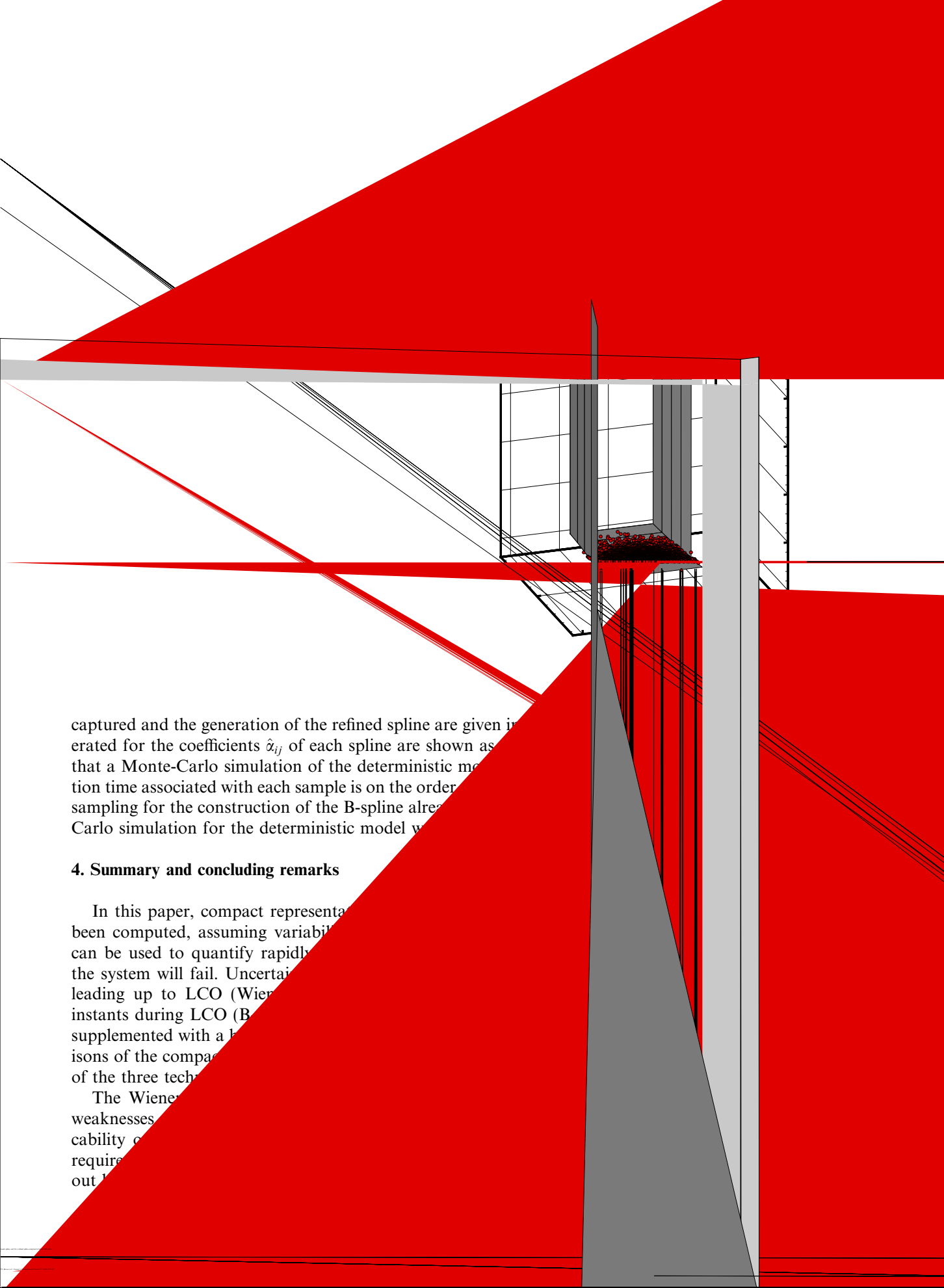
For the case of spring softening, a B-spline representation involving 60 samples is not adequate, but when the number of samples is increased to 180, the PDFs are in good quantitative agreement. It should be recalled that under subcritical conditions ($\lambda < \lambda^*$), two solutions are available: equilibrium (characterized by the algorithm as an LCO of zero amplitude) and large-amplitude LCO. Thus, the PDF is bi-modal in character, with a spike at zero amplitude. With a 180 samples, the B-spline technique effectively captures the bi-modal nature of the PDF, and does an excellent job of predicting very small probabilities in between the basic sets of solutions. It should be noted that the increase in computational time needed to obtain 4000 samples of the deterministic model is a result of needing longer run times to differentiate properly the character of the time-asymptotic solution.

3.4.2. High-order airfoil model

A related aeroelastic airfoil model is studied, assuming that the airloads are computed with CFD (discrete Euler equations). This constructed model is described by Millman [27], the reference the reader should consult to obtain details of the procedure and its verification. To justify the use of a high-fidelity physics representation of the aerodynamics, the structurally supported airfoil is suspended in an airstream at Mach 0.85, leading to the generation of shocks that move adjacent to the airfoil as it dynamically changes its pitch and plunge orientation.

Owing to the new demands of the environment, alterations are made to the assumed values of the physical parameters to yield well-behaved LCO branches like that obtained for the low-order airfoil model (but at much smaller pitch angles to maintain the viability of the Euler computation). In particular, the nonlinear stiffness coefficients in torsion are increased (e.g., $k_5 = 500$) and structural damping is added to both the pitch and plunge dynamical equations. For the new conditions, a Hopf bifurcation at about $\lambda^* = 6.78$ is predicted. In the stochastic analysis, changes are also made in the distributions of α_0 and k_3 : $\alpha_0(\xi) = 1.5\xi$ (degrees) and $k_3(\xi_2) = -30 + 3\xi_2$, and 10,000 samples are computed to improve the statistical convergence of the MCS.

Surface plots (response surfaces) of the B-splined samples are shown in Fig. 18. Two multivariate splines are shown: a spline computed with an 8×4 array of nodes (obtained using the process described in the Formulation section), and a refined spline based on an irregular distribution of about 100 nodes that are selected to capture sharply the discontinuous, separatrix surface. Details of the process by which the surface is



captured and the generation of the refined spline are given in [16]. The coefficients $\hat{\alpha}_{ij}$ of each spline are shown as in Fig. 10. The computation time associated with each sample is on the order of 100 s. The sampling for the construction of the B-spline already includes a Monte-Carlo simulation for the deterministic model with

4. Summary and concluding remarks

In this paper, compact representations of the failure probability have been computed, assuming variability in the input parameters. These can be used to quantify rapidly the reliability of a system and the time the system will fail. Uncertainty in the input parameters, leading up to LCO (Wiener process) and the time instants during LCO (B-spline) are considered. The model is supplemented with a hierarchical structure. The results of the comparisons of the compact representations and the full model of the three techniques are presented in Fig. 11.

The Wiener process has several weaknesses. The computation of the reliability of a system requires a large number of Monte-Carlo simulations. The out-

Table 2
Comparison of stochastic methods for LCO (strengths)

| Cyclic (response) | Wiener–Haar (response) | B-spline (amplitude) |
|------------------------|----------------------------|----------------------------|
| Rapid P -convergence | Resolution of nonlinearity | Resolution of nonlinearity |
| Low deterministic cost | Unsteady (non-LCO) | Non-intrusive |

Table 3
Comparison of stochastic methods for LCO (weaknesses)

| Cyclic (response) | Wiener–Haar (response) | B-spline (amplitude) |
|-------------------|------------------------|----------------------|
| LCO only | Complexity (intrusive) | LCO amplitude only |
| ICs not random | Dimensionality | |

Owing to the limits of the responses captured by the Cyclic and B-spline projection techniques, the Wiener–Haar approach shows the most promise for general, unsteady applications, e.g., those applications not leading to simple LCO. In such cases, the assumption of time periodicity breaks down and it becomes more difficult to pick particular conditions that would characterize failure. For example, peak pitch angle becomes a less significant measure of overall vehicle safety. In this sense, stochastic analysis of all available data becomes more important, since it is in this context that a variety of failure sources (e.g., loads, tip deflection, separation, etc.) can be simultaneously evaluated. It is, though, important to consider going beyond the Wiener–Haar projection of data to a tighter connection between the multi-dimensional basis and the time-integration algorithm, such as in the case of intrusive methods, or the equation-free approach suggested in [41].

For problems that predictably enter into LCO over a range of conditions (such as in a preliminary design process, where LCO would be removed through a reliability-based optimization), Cyclic methods, and their Harmonic Balance brethren, offer the most computationally efficient means of capturing LCO. LCOs obtained in this manner could then serve as a means for non-intrusively projecting onto compact bases using either B-spline or Wiener–Hermite techniques. Based on the demonstrated success of the B-spline approach to capturing jumps in response characteristics arising from a subcritical bifurcation, application of the B-spline projection method to peak responses obtained from cyclic data (i.e., non-intrusive) would seem to be the superior method. Also, as described above, WHa expansions may be incorporated into the Cyclic methodology. However, the key issue that remains to be addressed is how to link cyclic solutions with initial conditions (ICs). The stochastic projection of responses using the B-spline shown in this paper involved responses computed with a time-domain strategy. A similar mapping of input-to-output characteristics, including initial conditions, needs to be developed for the Cyclic method. As is the case with the Wiener–Haar projection, further work needs to be carried out to determine if an intrusive Cyclic strategy can be made viable (i.e., more efficient than a non-intrusive approach).

Finally, it is worth noting that each of the proposed methods appears to work well when the number of sources of variability is limited. However, it is hard to determine how each of these techniques might be generalized to handle large numbers of variable parameters, such as when a variability is distributed, or when a system is highly complex. This comment is especially applicable to methodologies in which the stochastic characteristics of input variables need to be explicitly represented, as is true of intrusive techniques. The cyclic techniques, which were constructed using a single rv of standard normal distribution, may most readily be extended to treat multiple Gaussian variables, whereas this generalization may prove more challenging for the Wiener–Haar approach. Recent work (cf. [18]) has examined the application of multi-resolution methods to problems involving multiple stochastic dimensions; however more work needs to be done to overcome the greatly increased cost of these computations.

Acknowledgments

The authors gratefully acknowledge the support of the Air Force Office of Scientific Research under Grant 03VA01COR (Dr. Fariba Fahroo, Program Manager). The authors also thank Dr. Chuck Denegri, Jr., for many helpful discussions concerning the LCO properties of existing air vehicles systems and the relevance of uncertainty in these systems.

References

- [1] P.J. Attar, E.H. Dowell, A stochastic analysis of the limit cycle behavior of a nonlinear aeroelastic model using the response surface method, AIAA 2005-1986, April, 2005.
- [2] P.S. Beran, C.L. Pettit, A direct method for quantifying limit-cycle oscillation response characteristics in the presence of uncertainties, in: 45th AIAA/ASCE/AHS/ASC Structures, Structural Dynamics, and Materials Conference, AIAA 2004-1695, April, 2004.
- [3] P.S. Beran, D.J. Lucia, A reduced order cyclic method for computational of limit cycles, *Nonlinear Dynamics* 39 (1–2) (2005) 143–158.
- [4] P.S. Beran, N.S. Khot, F.E. Eastep, R.D. Snyder, J.V. Zweber, Numerical analysis of store-induced limit-cycle oscillation, *J. Aircraft* 41 (6) (2004) 1315–1326.
- [5] R.W. Bunton, C.M. Denegri Jr., Limit cycle oscillation characteristics of fighter aircraft, *J. Aircraft* 37 (5) (2000) 916–918.
- [6] A.M. Cunningham Jr., Practical problems: airplanes, in: David Nixon (Ed.), *Unsteady Transonic Aerodynamics*, American Institute of Aeronautics and Astronautics, 1989.
- [7] C. de Boor, *A Practical Guide to Splines*, revised ed., Springer, New York, 2001.
- [8] C.M. Denegri Jr., J.A. Dubben, F-16 Limit cycle oscillation analysis using transonic small-disturbance theory, AIAA 2005-2296, April, 2005.
- [9] E.J. Doedel, AUTO: a program for the automatic bifurcation analysis of autonomous systems, in: *Proceedings of the 10th Manitoba Conf. on Numerical Math. and Comp., Cong. Num. vol. 30*, 1981, pp. 265–284.
- [10] E.H. Dowell, K.C. Hall, Modeling of fluid–structure interaction, *Ann. Rev. Fluid. Mech.* 33 (2001) 445–490.
- [11] C. Farhat, P. Geuzaine, G. Brown, C. Harris, Nonlinear flutter analysis of an F-16 in stabilized, accelerated, and increased angle of attack flight conditions, AIAA 2002-1490, April, 2002.
- [12] C. Gasquet, P. Witomski, *Fourier Analysis and Applications: Filtering, Numerical Computation, Wavelets*, Springer, New York, 1999.
- [13] R. Ghanem, P.D. Spanos, *Stochastic Finite Elements: A Spectral Approach*, revised ed., Dover Publications, New York, 2003.
- [14] K.C. Hall, J.P. Thomas, W.S. Clark, Computation of unsteady nonlinear flows in cascades using a harmonic balance technique, in: *International Symposium on Unsteady Aerodynamics, Aeroacoustics and Aeroelasticity of Turbomachines and Propellers*, Lyon, France, September, 2000.
- [15] M. Holodniok, M. Kubicek, DERPER – an algorithm for the continuation of periodic solutions in ordinary differential equations, *J. Comput. Phys.* 55 (1984) 254–267.
- [16] B. Lee, L. Jiang, Y. Wong, Flutter of an airfoil with a cubic restoring force, AIAA 1998-1725, April, 1998.
- [17] O.P. Le Maitre, O.M. Knio, H.N. Najm, R.G. Ghanem, Uncertainty propagation using Wiener–Haar expansions, *J. Comput. Phys.* 197 (2004) 28–57.
- [18] O.P. Le Maitre, H.N. Najm, R.G. Ghanem, O.M. Knio, Multi-resolution analysis of Wiener-type uncertainty propagation schemes, *J. Comput. Phys.* 197 (2004) 502–531.
- [19] N. J Lindsley, P.S. Beran, C.L. Pettit, Effects of uncertainty on nonlinear, 3-DOF plate aeroelastic response, AIAA 2002-1271, April, 2002.
- [20] N. J Lindsley, P.S. Beran, C.L. Pettit, Effects of uncertainty on the aerothermoelastic flutter boundary of a nonlinear plate, AIAA 2002-5136, September–October, 2002.
- [21] N. J Lindsley, P.S. Beran, Increased efficiency in the stochastic interrogation of an uncertain nonlinear aeroelastic system, in: *International Forum on Aeroelasticity and Structural Dynamics*, Munich, Germany, IF-055, June, 2005.
- [22] S. Mallat, *A Wavelet Tour of Signal Processing*, second ed., Academic Press, New York, 1999.
- [23] M. McMullen, A. Jameson, J. Alonso, Application of a non-linear frequency domain solver to the Euler and Navier–Stokes equations, AIAA 2002-0120, January, 2002.
- [24] M.E. Melchers, *Structural Reliability Analysis and Prediction*, Wiley, New York, 1999.
- [25] D.R. Millman, P.I. King, P.S. Beran, A stochastic approach for predicting bifurcation of a pitch and plunge airfoil, AIAA 2003-3515, June, 2003.
- [26] D.R. Millman, P.I. King, R.C. Maple, P.S. Beran, Predicting uncertainty propagation in a highly nonlinear system with a stochastic projection method, in: 45th AIAA/ASCE/AHS/ASC Structures, Structural Dynamics, and Materials Conference, AIAA 2004-1613, April, 2004.
- [27] D.R. Millman, Quantifying initial condition and parametric uncertainties in a nonlinear aeroelastic system with an efficient stochastic algorithm, Ph.D. Dissertation, Air Force Institute of Technology, September, 2004.
- [28] D.R. Millman, P.I. King, P.S. Beran, Airfoil pitch-and-plunge bifurcation behavior with Fourier chaos expansions, *J. Aircraft* 42 (2) (2005) 376–384.
- [29] C.L. Pettit, P.S. Beran, Effects of parametric uncertainty on airfoil limit cycle oscillation, *J. Aircraft* 40 (5) (2003) 1004–1006.
- [30] C.L. Pettit, P.S. Beran, Polynomial chaos expansion applied to airfoil limit cycle oscillations, AIAA 2004-1691, April, 2004.
- [31] C.L. Pettit, Uncertainty quantification in aeroelasticity: recent results and research challenges, *J. Aircraft* 41 (5) (2004) 1217–1229.
- [32] C.L. Pettit, P.S. Beran, Wiener–Haar expansion of airfoil limit cycle oscillations, AIAA 2005-1985, April, 2005.
- [33] C.L. Pettit, P.S. Beran, Convergence studies of Wiener expansions for computational nonlinear mechanics, in: Abstract submitted to the 47th AIAA/ASCE/AHS/ASC Structures, Structural Dynamics, and Materials AIAA 2006–1993, May, 2006.
- [34] C.L. Pettit, P.S. Beran, Wiener expansions of oscillatory stochastic processes, *J. Sound Vibr.* 294 (4–5) (2006) 752–779.
- [35] J.P. Thomas, E.H. Dowell, K.C. Hall, Modeling viscous transonic limit cycle oscillation behavior using a harmonic balance approach, AIAA 2002-1414, April, 2002.

- [36] J.P. Thomas, E.H. Dowell, K.C. Hall, C.M. Denegri Jr., Further investigation of modeling limit cycle oscillation behavior of the F-16 fighter using a harmonic balance approach, AIAA 2005-1917, April, 2005.
- [37] J.P. Thomas, E.H. Dowell, K.C. Hall, C.M. Denegri Jr., An investigation of the sensitivity of F-16 fighter limit cycle oscillations to uncertainties, in: Abstract submitted to the 47th AIAA/ASCE/AHS/ASC Structures, Structural Dynamics, and Materials Conference (May 2006), August, 2005.
- [38] X. Wan, G.E. Karniadakis, An adaptive multi-element generalized polynomial chaos method for stochastic differential equations, *J. Comput. Phys.* 209 (2005) 617–642.
- [39] D. Xiu, G.E. Karniadakis, The Wiener–Askey polynomial chaos for stochastic differential equations, *SIAM J. Sci. Comput.* 24 (2) (2002) 619–644.
- [40] D. Xiu, D. Lucor, C.H. Su, G.E. Karniadakis, Stochastic modeling of flow–structure interactions using generalized polynomial chaos, *J. Fluids Eng.* 124 (2002) 51–59.
- [41] D. Xiu, I.G. Kevrekidis, R. Ghanem, An equation-free, multiscale approach to uncertainty quantification, *Comput. Sci. Eng.* (May/June) (2005) 16–23.